The 3D genomics of lampbrush chromosomes highlights the role of active transcription in chromatin organization

T. Lagunov*[,1,2], M. Gridina*[,1,2], A. Nurislamov[1,2,5], T. Kulikova[3], A. Maslova[3], V. Konstantinov[1,2], A. Popov[1,4], A. Krasikova[3,+], V. Fishman[1,2,4,5,+]

1 - Institute of Cytology and Genetics, Novosibirsk, Russia
2 - Novosibirsk State University, Novosibirsk, Russia
3 - Laboratory of Cell Nucleus Structure and Dynamics, Saint-Petersburg State University, Saint-Petersburg, Russia
4 - Artificial Intelligence Research Institute, Moscow, Russia
5 - Sirius University of Science and Technology, Sirius, Russia
*-equal contribution
[+]-correspondence should be sent to Veniamin Fishman (minja-f@yandex.com) and Alla Krasikova (alla.krasikova@gmail.com)

Abstract

Lampbrush chromosomes are giant meiotic bivalents in growing oocyte nuclei that have served as a classic model system for studying chromatin organization and RNA synthesis for over a century. Despite their importance, the molecular mechanisms underlying lampbrush chromosomes formation and their distinctive chromomere-loop architecture have remained poorly understood. Here, we provide the first comprehensive genomic, cytological, and biophysical analysis of lampbrush chromosome organization by integrating single-cell Hi-C, RNA-seq, NOMe-seq, FISH mapping, and chromatin simulations. Single-nucleus Hi-C analysis revealed CTCF-independent contact domains with stable boundaries defined by transcription units in a convergent orientation. Contact domains identified through Hi-C analysis correspond to insulated chromomeres in lampbrush chromosomes. Small transcriptionally inactive contact domains surrounded by transcription units in the diverged orientation form ‘chromatin knots’, which are often detached from the chromosome axis. Transcription loops frequently manifest as a 'cross' pattern with reduced contacts within chromatin domains. Integrative analysis of the whole-genome data uncovers the mechanisms underlying lampbrush chromosome structure, revealing how hypertranscription modulates chromatin stiffness and repositions SMC complexes to establish the distinctive chromomere-loop organisation. Biophysical modeling through polymer simulation reproduces key features of lampbrush chromosomes, including transcription loop formation, chromomere compaction, and insulation patterns. These findings offer a unifying framework for understanding the remarkable chromatin architecture of lampbrush chromosomes and their transcription-dependent organization.

Highlights

- First integration of single-cell Hi-C, RNA-seq, NOMe-seq and microscopy methods uncovers molecular mechanisms underlying lampbrush chromosome architecture.
- Hi-C reveals contact patterns corresponding to lampbrush chromomeres and transcription loops, validated through BAC-based FISH mapping.
- Lampbrush chromosomes are segmented into contact domains formed via a CTCF-independent mechanism, with boundaries coinciding with convergently oriented gene pairs.
- Hypertranscription shapes lampbrush chromosome through multiple mechanisms, increasing stiffness and decreasing compaction of transcribed units, generating outward pressure, pushing transcription loops away from the chromosome axis, and repositioning SMC complexes to form transcription-dependent domains with stable boundaries.
- Polymer simulations including these mechanisms replicate key features of LBC organization, supporting the proposed model of lampbrush chromosomes formation.

Key words

Chromatin architecture, chromatin domain, chromomere, cohesion, contact domain, hypertranscription, lampbrush chromosomes, loop extrusion, oocyte nucleus, polymer simulation, single-cell Hi-C, transcription loops

Graphical Abstract

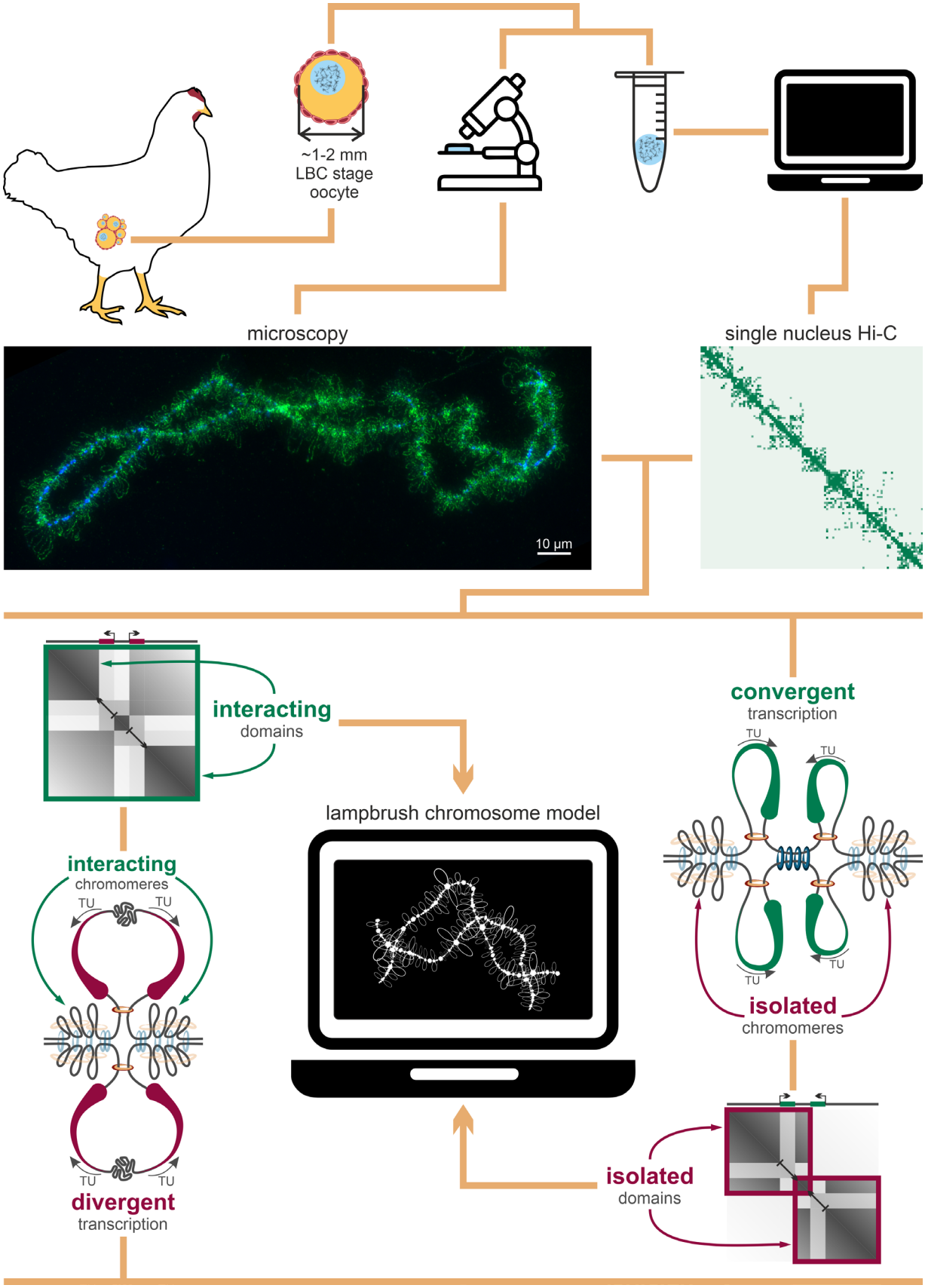

Main

Chromosomes are folded non-randomly in the nuclear space. Their spatial organization is essential for several genomic processes ([1–3]), such as regulation of gene expression ([4–7]), DNA replication ([8–10]) and repair ([11]), and mechanical properties of the nucleus ([12,13]). Consistent with this pivotal role in genome regulation, spatial organization of chromatin was shown to be conserved across large evolutionary distances of hundreds of million years ([14–17]).

There are several essential mechanisms responsible for chromatin organization in animal cells. First, DNA is a polymer organized in the nuclear space according to the principles of polymer physics. This implies that frequency of contacts between loci decreases with increase of genomic distance, following power law. For the majority of the studied cell types, scaling of contacts with genomic distance is concordant with the fractal globule model of the DNA packaging, characterized by a fractal dimension of ~3 ([18]). Second, multivalent homotypic interactions between proteins cause segregation of the chromatin into compartments with distinct epigenetic states ([19–23]). Moreover, active and inactive chromatin is directed towards different nuclear landmarks ([2]). Inactive chromatin is often associated with nuclear lamina and nucleolar periphery, while active chromatin is in proximity to the interchromatin space comprising nuclear speckles ([24–26]). Third, ATP-dependent extrusion of DNA by SMC-complexes cohesin and condensin results in chromosome compaction and increased probability of long-range interactions ([1,27,28]). The extrusion process can be modulated by several factors. In the majority of vertebrate cell types, CTCF protein blocks cohesin-mediated extrusion, therefore CTCF binding sites demarcate compact self-interacting genomic regions, often referred to as topologically associated domains (TADs) ([1,29–32]). Interactions of cohesin with other proteins, including replication-specific MCM ([33]) or transcription-associated RNA-polymerase II complexes ([34–37]) also may modulate extrusion, although details of these mechanisms are less studied. Moreover, interaction of cohesin with MCM and RNA-polymerase have less impact on genomic contacts compared to cohesin-CTCF interactions, and require artificial modulation ([36]) or analysis of specific cell cycle stages ([33]) to be observed.

Although chromatin contacts in the majority of vertebrate cells can be explained by above mentioned mechanisms with relatively high accuracy ([38,39]), specific cell types or cell cycle stages show distinct arrangement of chromatin ([2]). This includes early stages of development, prior to or immediately after zygotic genome activation, and germ cells ([40]). Importantly, chromatin architecture is uniquely reorganized during the oocyte-to-zygote transition. In mammals, features of genomic organization at diplotene stage include compartments, TADs, and loops ([40,41]). Although these chromatin domains can be detected when averaged over the genome, the presence of each type of domain at a locus varies between cells ([41]). TAD boundaries in murine oocytes are located concordant with somatic cells, demarcated by CTCF, and associated with cohesin-mediated loop extrusion ([41]). Compartments in murine diplotene oocytes manifest as plaid-pattern of Hi-C contacts and demonstrate strong association with distribution of H3K27me3 mark ([40]). Compared to somatic cells, in oocytes interactions within compartments are restricted to the regions located less than 10 Mb away from each other, presenting a “local compartmentalization” pattern ([40]). Similar depletion of long-range interactions and local

compartmentalization was also observed during meiotic division of sperm cells ([42,43]). Strength of both TADs and compartments gradually decreases with oocyte transition from early to late diplotene stage, and these structures disappear at metaphase-II (MII) stage ([40,41]).

Previous whole-genomic studies focused on chromatin organization in oocytes did not include representatives of vertebrate taxa in which chromatin undergoes lampbrush chromosome state. Lampbrush chromosomes (LBCs) represent a specific form of nuclear chromatin that emerges at the diplotene stage of oogenesis in the majority of vertebrate species, including amphibians, fish, reptiles, birds (Figure 1B), monotremes, and certain insects. In the 3D space of the giant oocyte nucleus, lampbrush chromosomes do not contact each other, are not tethered to the nuclear periphery, and do not have a preferred radial position ([44,45]). Lampbrush chromosomes consist of separate chromatin globules connected by a thin thread and protruding lateral loops, together forming chromomere-loop complexes ([46–48]). The unusually enormous size of LBCs allows for chromomere-loop structure visualization using conventional light microscopy, making diplotene oocytes a preferred model for microscopy-based studies of chromatin architecture.

The phenomenon of LBC organization is attributed to hypertranscriptional activity of the oocyte nucleus ([49,50]). Hypertranscription results in formation of lateral loops tightly covered by elongating RNA polymerases and nascent transcripts ([48,51,52]) and containing single or multiple genes essential for maternal products biosynthesis ([53–56]). Another structural unit of LBC are lampbrush chromomeres ([47]). Chromomeres do not clearly correspond to any of the known spatial chromatin domains of the interphase nucleus. Genomic loci of neighbouring somatic TADs can be detected as a part of a single chromomere, while genomic regions belonging to one somatic TAD can be detected as a part of two adjacent chromomeres ([54,57]). There is, however, partial correspondence between gene-poor heterochromatic regions of constitutive B-compartments identified in somatic cells and clusters of large DAPI-positive chromomeres, which are also enriched for inactive chromatin marks ([57–61]).

Overall, chromatin organization in LBCs drastically differs from somatic cells, asking whether there are unique mechanisms of genome architecture that are active at this stage.

Here, we present the first Hi-C analysis of lampbrush chromosomes, supplemented by transcriptomic and epigenomic profiling. We show that chromatin contacts in LBCs display unique features, including restriction of long-range and inter-chromosomal interactions and formation of CTCF-independent chromatin domains and loops. We show strong correlation between location and orientation of transcription units and formation of chromatin domain boundaries. Based on our observations, validated by FISH and other complementary analysis, we develop a physical model of LBCs explaining LBC architecture via interplay between SMC and RNA-polymerase complexes. We show that the polymer model can qualitatively explain observed Hi-C patterns genome-wide and accurately reproduce spatial configuration of individual loci. Finally, the developed model highlights the importance of the transcription-mediated ribonucleoprotein matrix accumulation and nucleosome removal as factors determining spatial structure of LBC.

Results

Isolation and quality control of chicken diplotene oocytes

To investigate chromatin organization in avian lampbrush chromosomes, we selected chicken oocytes at the lampbrush stage based on follicle size. Individual nuclei were isolated and processed using a previously established single-cell Hi-C protocol ([62]) (Figure 1A). Multiple quality control measures were conducted to validate the integrity and reliability of the resulting data.

To confirm that formaldehyde fixation preserves the lampbrush chromosome structure, we stained fixed nuclei with SYTO 61 dye and visualized them using confocal microscopy. The analysis demonstrated the characteristic lampbrush morphology of the captured chromosomes (Figure 1C), consistent with previous findings ([44]).

Next, we ensured that oocyte genomic material was not contaminated by somatic cells. Chicken follicles include various cell types, such as erythrocytes, which are significantly smaller than oocyte nuclei. To exclude contamination, nine randomly selected oocyte nuclei were stained with DAPI post-isolation and visually inspected. Microscopy analysis revealed no DAPI signals outside oocyte chromosomes. As a control, erythrocytes were manually added to oocyte samples, confirming that erythrocyte nuclei are detectable during visual inspection (Supplementary Figure S1A, B).

To further validate the absence of contamination, we leveraged the fact that a single oocyte nucleus contains no more than four copies of each genomic fragment. Consequently, no more than eight unique interactions should be detected per *Dpn*II restriction fragment (two ends per fragment, [63]). Genomic fragments exhibiting more than eight interactions would indicate contamination or Hi-C artifacts. Our analysis showed that the vast majority of fragments exhibit fewer than nine interactions (Supplementary Figure S1E). These results confirm that the isolated oocyte nuclei were free of contamination from other chicken cell types.

Single-nucleus Hi-C experiments were performed on a total of 96 oocyte nuclei. Initial library quality was evaluated through shallow sequencing (~200,000 reads per sample), using metrics such as the fraction of unmapped reads, duplicate reads, intra-chromosomal reads, and intra-fragment reads (see “Methods”). Based on these criteria, 25 single-cell oocyte libraries were selected for deeper sequencing (~3–40 million read pairs per nucleus) and downstream analysis (Supplementary Table S1).

The resulting Hi-C maps achieved >80% bin coverage at 4 Kb resolution for most samples, with a few exceptions where one or more chromosomes were completely absent but the remaining genome showed consistent coverage (Supplementary Figure S1D). Deeply sequenced Hi-C maps displayed a high degree of similarity across individual oocyte nuclei (Figure 3A, B), confirming the high quality of the obtained data.

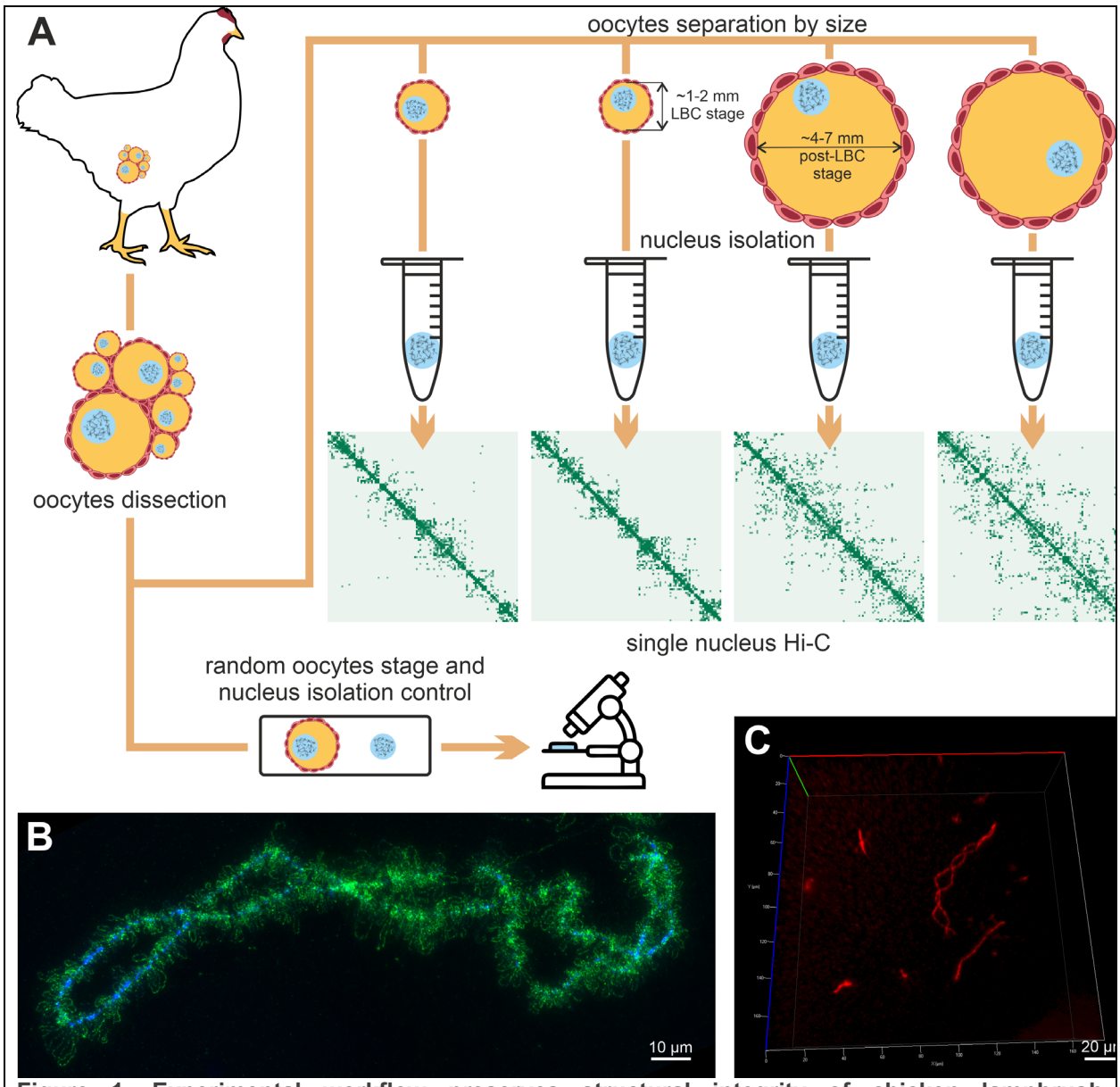

Figure 1. Experimental workflow preserves structural integrity of chicken lampbrush chromosomes.
A) Experimental workflow, including oocyte dissection, oocytes separation by size (lampbrush chromosome stage oocytes: 1–2 mm diameter; post-lampbrush chromosome stage oocytes: 4–7 mm diameter), microsurgical isolation of nuclei, and preparation of single-nucleus Hi-C libraries. Selected oocytes and nuclei were randomly chosen for quality control.
B) Chromomere-loop structure of isolated chicken lampbrush chromosome 1. Elongating RNA polymerase II is labeled with antibodies (green), and chromatin is counterstained with DAPI (blue).
C) Lampbrush chromosomes preserve their 3D-structure after formaldehyde fixation. The entire nucleus is visualized after fixation and staining with SYTO 61.

Lampbrush chromosomes form elongated structures with minimal inter-chromosomal interactions

Lampbrush bivalents at the diplotene stage of meiosis are known to form elongated structures that are spatially separated within the giant oocyte nucleus ([44]). This spatial arrangement is also preserved after fixation, as shown in Figure 1C. Hi-C data analysis further confirms these unique features of LBCs.

Our results show a strikingly low frequency of inter-chromosomal (trans) contacts, with only 0.2–1% of spatial interactions occurring between non-homologous chromosomes (Supplementary Table S1). This is markedly lower than the ~10% reported for chicken fibroblasts ([15]) and the 10–30% typical of somatic cells in various species ([14,64]). These data underscore the exceptional rarity of inter-chromosomal interactions in lampbrush-stage oocytes (Supplementary Table S1).

Intra-chromosomal (cis) interactions in lampbrush chromosomes exhibit an abrupt drop in contact frequency beyond ~1 Mb (Figure 2), consistent with the elongated, rope-like morphology of these chromosomes (Figure 1B). The depletion of both long-range and trans-chromosomal interactions in LBC Hi-C maps results in the absence of the plaid-pattern of contacts typically observed in interphase nucleus Hi-C data, which is associated with chromatin compartmentalization ([65]).

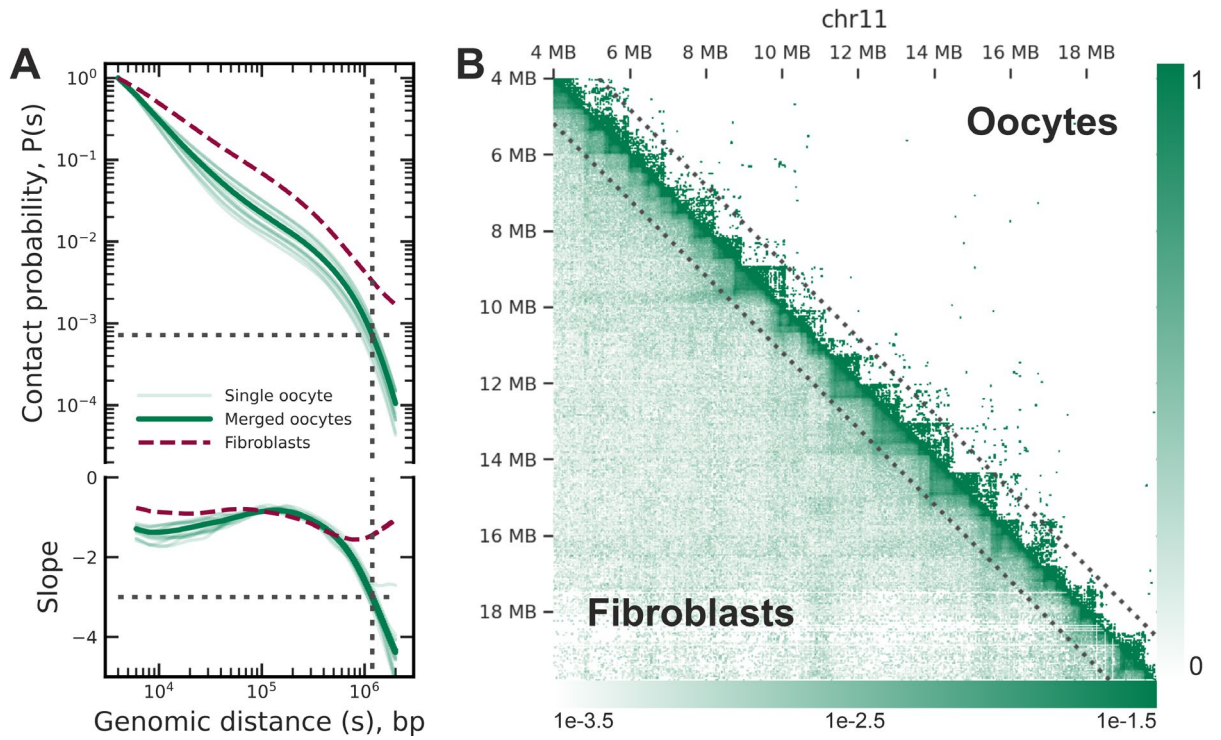

Figure 2. Chromatin organization of lampbrush chromosomes at different genomic distances.
A) Contact probability versus the genomic distance for single and merged oocyte data (lampbrush chromosome stage). The dashed line indicates dependence typical for the fractal dimension of 1 (slope equals -3).
B) Hi-C contact map of chicken oocytes against Hi-C map of fibroblasts cells (chr11). The dashed line indicates the genomic distance when observed slope is similar to the expected for the polymer with fractal dimension 1.

Chromatin of lampbrush chromosomes forms domains with stable boundaries shared across individual oocytes

In contrast to the absence of a plaid-pattern, chromatin domains are clearly visible on LBC Hi-C maps at scales of 0.5–2 Mb (Figure 2B and 3B-D).

In mouse diplotene oocytes at the non-surrounded nucleolus (NSN) stage, chromatin interaction analysis reveals TADs with highly variable boundary locations across

individual cells ([41]). In contrast, single-nucleus Hi-C maps from chicken lampbrush-stage oocytes demonstrate striking consistency in domain boundary positions (Figure 3A-C), with a mean F1 score of 0.48 compared to 0.23 for mouse NSN oocytes (Figure 3A). This stability in domain boundaries across chicken LBCs suggests fundamental differences in the mechanisms underlying chromatin domain formation between these two systems.

Contact domains in LBCs can be classified into two types based on their length (Figure 3D,E): 1) Large Unstructured Domains (LUDs), defined as domains longer than 1.3 Mb (N50 of domains length, see “Methods”) and 2) Small Squared Domains (SSDs), shorter than 1.3 Mb. Visually, LUDs have more dispersed contacts that are connecting loci up to ~2 Mb from each other (Figure S7A,B). Almost all LUDs are located on macro (chr1-chr5) and Z chromosomes (Figure 3H).

To characterize chromatin states in LUDs and SSDs, we performed a single cell NOMe-seq experiment, enabling simultaneous analysis of chromatin accessibility and CpG methylation levels in individual nuclei (CpG methylation was obtained from NOMe-seq experiment and from [[66]], see “Methods”). We also quantified transcription levels, reanalyzing RNA-seq data from the previous chicken oocyte nucleus transcriptome study ([56]) and supplementing it with additional replicas generated in this work. Analysis of these data shows that LUDs have lower median gene density (Supplementary Figure S2D) and lower normalized expression levels than SSDs (Figure 3G). We found that SSDs have significantly higher levels of GpC methylation, indicating that shorter domains contain more accessible chromatin (Supplementary Figure S2F), while there is almost no difference in CpG methylation levels between SSDs and LUDs (Figure 3F, Figure S2E), as well as only a weak correlation between promoter methylation and gene expression levels (Supplementary Figure S11).

Our findings indicate that Large Unstructured Domains correspond to gene-poor, transcriptionally inactive chromatin regions predominantly found on macrochromosomes and the Z chromosome. In contrast, Small Squared Domains are associated with gene-rich, transcriptionally active chromatin regions distributed across all chromosomes.

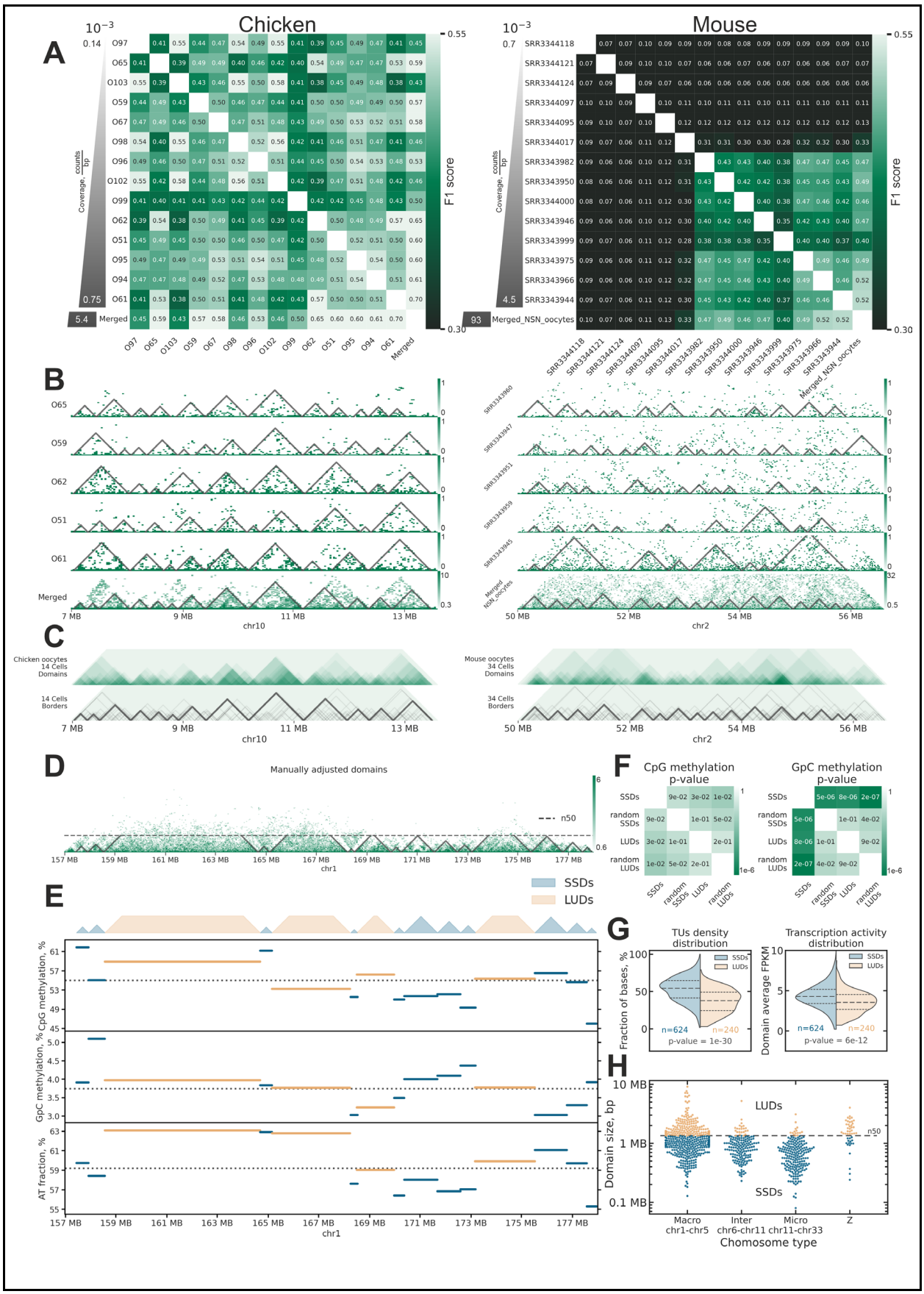
A
Chicken
Mouse
F1 score
Coverage, counts/bp
B
C
Chicken oocytes 14 Cells Domains
14 Cells Borders
Mouse oocytes 34 Cells Domains
34 Cells Borders
D
Manually adjusted domains
n50
E
SSDs
LUDs
CpG methylation, %
GpC methylation, %
AT fraction, %
F
CpG methylation p-value
GpC methylation p-value
G
TUs density distribution
Transcription activity distribution
Fraction of bases, %
Domain average FPKM
p-value = 1e-30
p-value = 6e-12
H
Domain size, bp
Macro chr1-chr5
Inter chr6-chr11
Micro chr11-chr33
Z
Chomosome type

239

Figure 3. Chromatin domains in chicken lampbrush chromosomes.
A) Pairwise F1 scores for domain boundary concordance across individual oocytes. Left panel: chicken lampbrush-stage oocytes; right panel: mouse NSN oocytes ([41]). Oocytes are sorted by the number of Hi-C contacts. Higher F1 scores indicate greater concordance in boundary positions. The mean F1 score is 0.48 for chicken oocytes and 0.23 for mouse oocytes. See Supplementary Figures S3–S6 and methods for additional details.
B) Domain annotations for individual cells and merged Hi-C data for chicken (left) and mouse (right) oocytes. Note the higher concordance of domain boundaries in chicken oocytes compared to mouse oocytes.
C) Aggregated Hi-C contacts and domain annotations for 14 chicken oocytes (left) and 34 mouse oocytes (right).
D) Merged Hi-C data from chicken oocytes with domain annotations overlaid. Domains were manually refined after automatic annotation (see "Methods"). The dashed line indicates the N50 domain size (~1.3 Mb).
E) Each horizontal segment represents a single chromatin domain, with the Y-position of the line indicating the domain's average characteristic (CpG methylation, GpC methylation, or AT fraction, see "Methods"). The dashed horizontal line represents the genome-wide average for each characteristic. This visualization highlights the distinct properties of Large Unstructured Domains (LUDs) and Small Squared Domains (SSDs). The genome-wide CpG and GpC methylation distributions can be found in Supplementary Figure S2E. The genome-wide AT fraction distribution can be found in Supplementary Figure S7D.
F) CpG and GpC methylation levels statistically compared between SSDs and LUDs (see "Methods"). As a baseline, domains were randomly redistributed across the genome while preserving the number of intervals and their length distributions (indicated as 'random'). SSDs exhibit significantly higher GpC methylation levels, reflecting increased chromatin accessibility. The genome-wide CpG and GpC methylation distributions can be found in Supplementary Figure S2E.
G) The transcription units (TUs) density and activity distribution show that the SSDs contain significantly more TUs, and TUs with higher activity, than LUDs.
H) Distribution of LUDs and SSDs lengths on chicken chromosomes.

Hi-C patterns align with chromatin units of lampbrush chromosomes identified by microscopy analysis

Lampbrush chromomeres are compact chromatin structures enriched in self-interactions and insulated from neighboring regions. Based on this characteristic, we propose that SSDs and LUDs in single-nucleus Hi-C maps correspond to chromomeres in LBCs. Additionally, given their properties, we speculate that LUDs represent more compact, DAPI-positive chromomeres, while SSDs correspond to less compact, DAPI-negative chromomeres. Supporting this hypothesis, statistical analysis of the AT fraction in domains—reflecting the genomic proportion susceptible to DAPI staining—shows a weak but significant correlation between AT fraction and domain length (Spearman's R = 0.55, compared to R = 0.28 for randomly shuffled domains, Supplementary Figure S7D).

To further validate the correlation between domain types and DAPI staining in chromomeres, we analyzed sequence markers with known positions in cytological maps of chicken LBCs, primarily derived from DNA- and RNA-FISH experiments using specific BAC clones (Figure 4A). The distribution of LUDs and SSDs correlated with the arrangement of DAPI-positive and DAPI-negative chromomeres at certain regions of chromosomes. For instance, we observed multiple LUDs between markers W030P07 and W030B21, coinciding with a region enriched in DAPI-positive chromomeres (Figure 4A). However, the number of cytologically visible chromomeres and contact domains on Hi-C maps does not always match exactly, probably due to the limited resolution of microscopy analysis and/or errors in domain callers. Together with sparse availability of sequence

markers distinguishing chromomeres and resolution of cytological chromomere-loop maps this limited a genome-wide analysis of the relationship between SSDs, LUDs, and chromomeres.

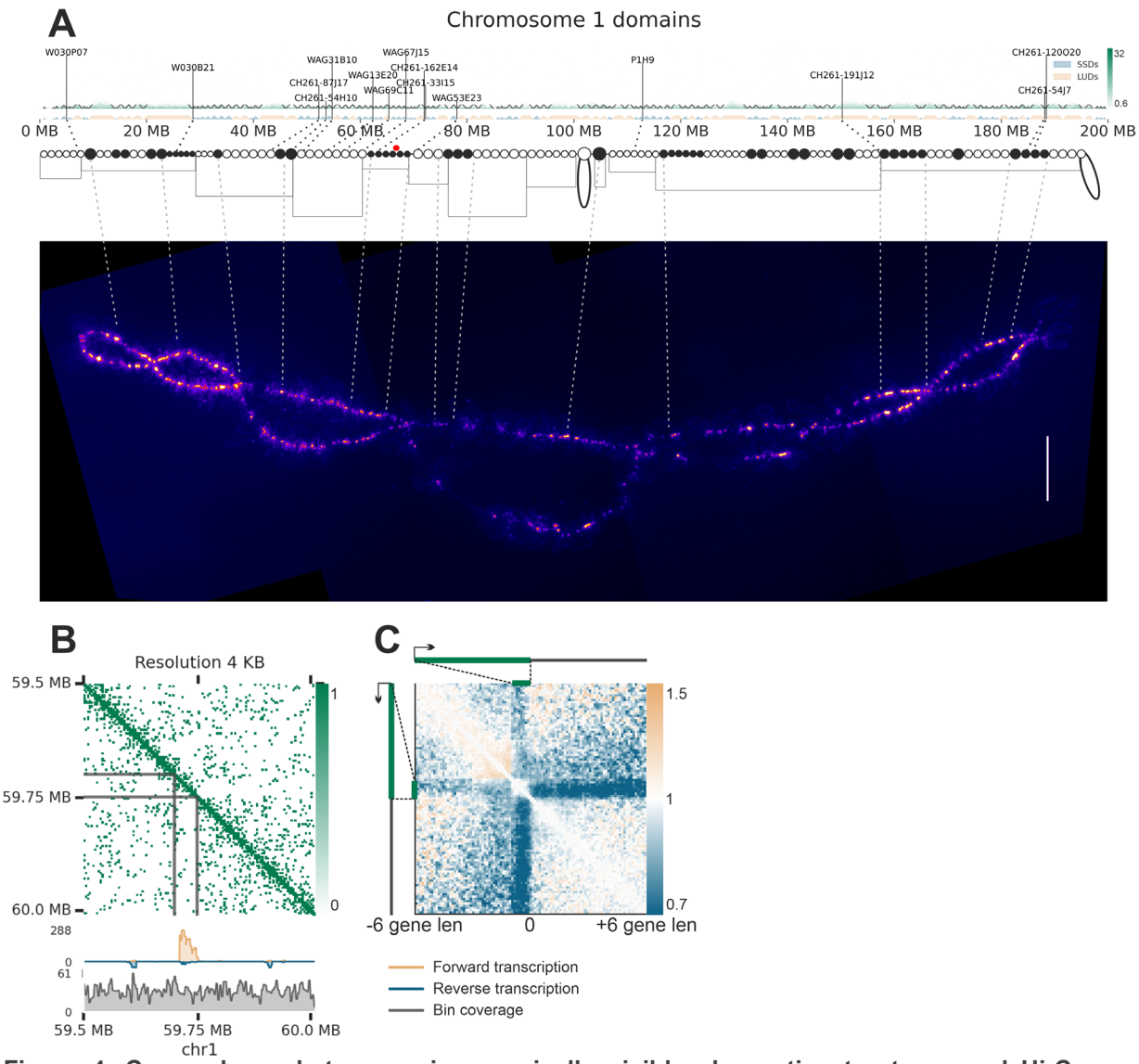

Figure 4. Concordance between microscopically visible chromatin structures and Hi-C map patterns along chicken lampbrush chromosomes

A) Comparison of Hi-C contact domains with chromatin domains identified through microscopy visualization of lampbrush chromosomes. From top to bottom: LBC Hi-C map for chicken chromosome 1, showing domain boundaries and DNA marker positions; Contact domain segmentation, with each triangle representing a single domain. LUDs and SSDs are distinguished by triangle colors, and black lines indicate DNA marker locations; Cytological map of chromomeres distribution along chicken lampbrush chromosome 1 ([67]), with DAPI-positive chromomeres shown as black circles and DAPI-negative chromomeres as white circles; the average lateral loop length in a region is shown by rectangles; DAPI-stained image of chicken lampbrush chromosome 1 (a fire look-up table corresponding to the intensity of fluorescence is used) (scale bar: 20 µm).

B) Hi-C map displaying an example of a “cross-like” pattern. The "cross" region overlaps with a high RNA-seq signal and shows no reduction in overall Hi-C coverage (denoted as "bin coverage").

C) Rescaled Hi-C map averaged around long (top 50% by length) and highly active (top 50% by FPKM) genes. A distinct "cross-like" pattern is observed, with flanking regions spanning ±6 gene lengths from the gene's end.

Transcription loops are a hallmark of lampbrush chromosomes. These loops represent stretched fibers of the actively transcribed chromatin emanating from the LBC axis. Given their spatial separation from each other and the LBC axis, we hypothesize that loci corresponding to transcription loops lack interactions with the rest of the genome.

Visual inspection of Hi-C maps reveals loci with a distinct "cross" pattern, where interactions are limited to nearest neighbors (Figures 4B,C). These loci compensate lack of long-range interactions by increasing frequency of proximal interactions, thus maintaining consistent coverage levels (Figure 4B). "Cross" patterns frequently occur within chromatin domains and almost always coincide with actively transcribed genes. Supporting this observation, aggregated Hi-C maps centered on long, highly expressed genes (top 50% by length and TPM) show a pronounced "cross" pattern (Figure 4C). These findings suggest that "cross" patterns in Hi-C maps represent the contact signatures of transcription loops in LBCs.

To align lampbrush chromatin contact patterns identified by Hi-C analysis with chromatin structures observable via microscopy, we conducted FISH mapping using probes specific to chromatin domain boundaries, internal domain regions, and loci forming “cross-like” patterns. A total of 29 BAC clones were hybridized in various combinations on lampbrush chromosomes 1, 4, and 13 (“Methods”, Supplementary Table S3). The large size of lampbrush chromosomes enables detailed microscopy analysis, allowing us to distinguish chromomeres and transcription loops, as well as determine the orientation of transcription units.

The locus analyzed on chromosome 1 contains six Hi-C domains. Regions 4, 6, 7, 9, and 12 coincide with "cross" patterns observed in Hi-C maps and the corresponding actively transcribed genes (Figure 5A). Based on the annotated transcription units' location and orientation, we anticipated transcription loops with forward-oriented transcription for regions 4, 9, and 12, and reverse-oriented transcription for regions 6 and 7. FISH mapping of LBC1 using BAC clone-based probes with a DNA+RNA hybridization protocol confirmed these predictions. Long lateral loops with a prominent RNP matrix were observed for BACs 4, 9, and 12, with transcription co-directional to the chromosome (Figure 5B, subpanels 2a, 3a-b). Similarly, genomic regions 6, 7, and 9, covered by three different BACs, correspond to transcription units forming one or two pairs of lateral loops (Figure 5B, subpanels 2c–e). BAC 5 doesn’t correspond to a region with an obvious “cross-like” pattern according to the Hi-C data, however it covers the transcriptionally active region (in reverse direction), thus it can form a transcription loop (Figure 5B subpanels 2a-b). In our FISH experiments, BAC 5 marks a reverse strand transcription loop anchored in the chromomere (Figure 5A,C). Additionally, RNA-FISH experiments without chromosomal DNA denaturation for several transcribed regions confirmed that BAC clone-based probes hybridize with nascent transcripts on the lateral loops. These findings confirm that "cross-like" patterns observed on Hi-C maps of avian LBCs correspond to the microscopically visible lampbrush lateral loops containing actively transcribed genes.

The intra-domain regions 1, 2, 3, 8, 10, and 14 correspond to five of the six contact domains identified on LBC Hi-C maps, with BACs 2 and 3 covering the same domain.

309 Consequently, we anticipated observing five insulated chromomeres along the
310 chromosome axis in microscopy images, one of which would be associated with two
311 BACs. FISH experiments confirmed this, with BAC clone-based probes mapping to five
312 distinct chromomeres (Figure 5B, subpanels 1a–b). The chromomeres covered by BAC
313 2 and BAC 3 are closely spaced but remain distinguishable (Figure 5B, subpanels 1c–d).

314 Interestingly, the compact chromatin domain covered by BAC 8, which lacks transcription,
315 exhibits variable positioning. This chromatin domain can either anchor directly to the
316 chromosome axis or remain detached from it (indicated by white arrows in Figure 5B),
317 forming a compact "knot" on a lateral loop emanating from the chromosomal axis. These
318 chromatin knots, located within transcriptionally active lateral loops, have been previously
319 described as small genomic regions devoid of transcribed genes (Figure 6 in [56]).

320 Together, these results demonstrate that (1) chromatin contact domains identified
321 through Hi-C analysis correspond to insulated chromomeres in lampbrush chromosomes,
322 and (2) small regions between actively transcribed genes can form microdomains (knots)
323 that are optionally tethered to the chromosomal axis.

324 Region 11 exhibits partial transcriptional activity and is positioned near the boundaries of
325 chromatin domains (Figure 5A). Based on this, we anticipated that BAC 11 would cover
326 a portion of chromatin spanning two adjacent chromomeres, one of which is covered by
327 BAC 10. FISH mapping confirmed this prediction, showing partial colocalization of BACs
328 10 and 11 within a prominent DAPI-positive chromomere (Figure 5B, subpanels 1a–d and
329 3d-e).

330 Similarly, BAC 13, located near the boundary of contact domain, produced a signal
331 spatially close to that of BAC 14, which maps to the same domain. While the signals from
332 BACs 13 and 14 are closely positioned, they remain distinct and do not intermix.

333 These results confirm that boundaries between domains identified by Hi-C are concordant
334 with LBC chromomere boundaries (see additional evidence supporting this statement in
335 the “Supplementary Note 2”).

336 On lampbrush chromosome 4, we mapped nine BAC clone-based probes across two
337 regions of interest. In region A (51–52 Mb), Hi-C data revealed the formation of a contact
338 domain with interactions at the top of the domain triangle and “cross-like” patterns within
339 domain, indicative of chromatin loop formation (Figure 5D). Nuclear RNA-seq data
340 showed that several genes within region A are transcribed in varying orientations. FISH
341 mapping confirmed that this genomic region corresponds to a long transcription loop with
342 multiple RNP matrix gradients (Figure 5E,F), consistent with the transcriptional activity
343 detected. Detailed results for region B are provided in “Supplementary Note 2” and
344 Supplementary Figure S8.

345 We integrated the FISH data to reconstruct the chromatin organization of the analyzed
346 region on chromosome 1 (Figure 5C), accounting for two alternative states of chromatin
347 knots discussed above. This reconstruction demonstrates a strong concordance between
348 microscopically visible chromatin structures—such as chromomeres and transcription
349 loops—and the contact domains and “cross-like” patterns observed in Hi-C maps. The

reconstruction of the region A on chromosome 4 also confirmed the correspondence between the transcription loops and the “cross-like” patterns (Figure 5D,E).

Additionally, similar analyses of two other regions on chromosomes 4 and 13, which included BACs mapped to Hi-C domain boundaries, intra-domain fragments, and “cross-like” patterns, yielded consistent results (Supplementary Figure S8; “Supplementary Note 2”). These findings validate the Hi-C maps of chicken oocyte nuclei and confirm the interpretation of Hi-C patterns as representations of lampbrush chromosome chromomeres and lateral loops.

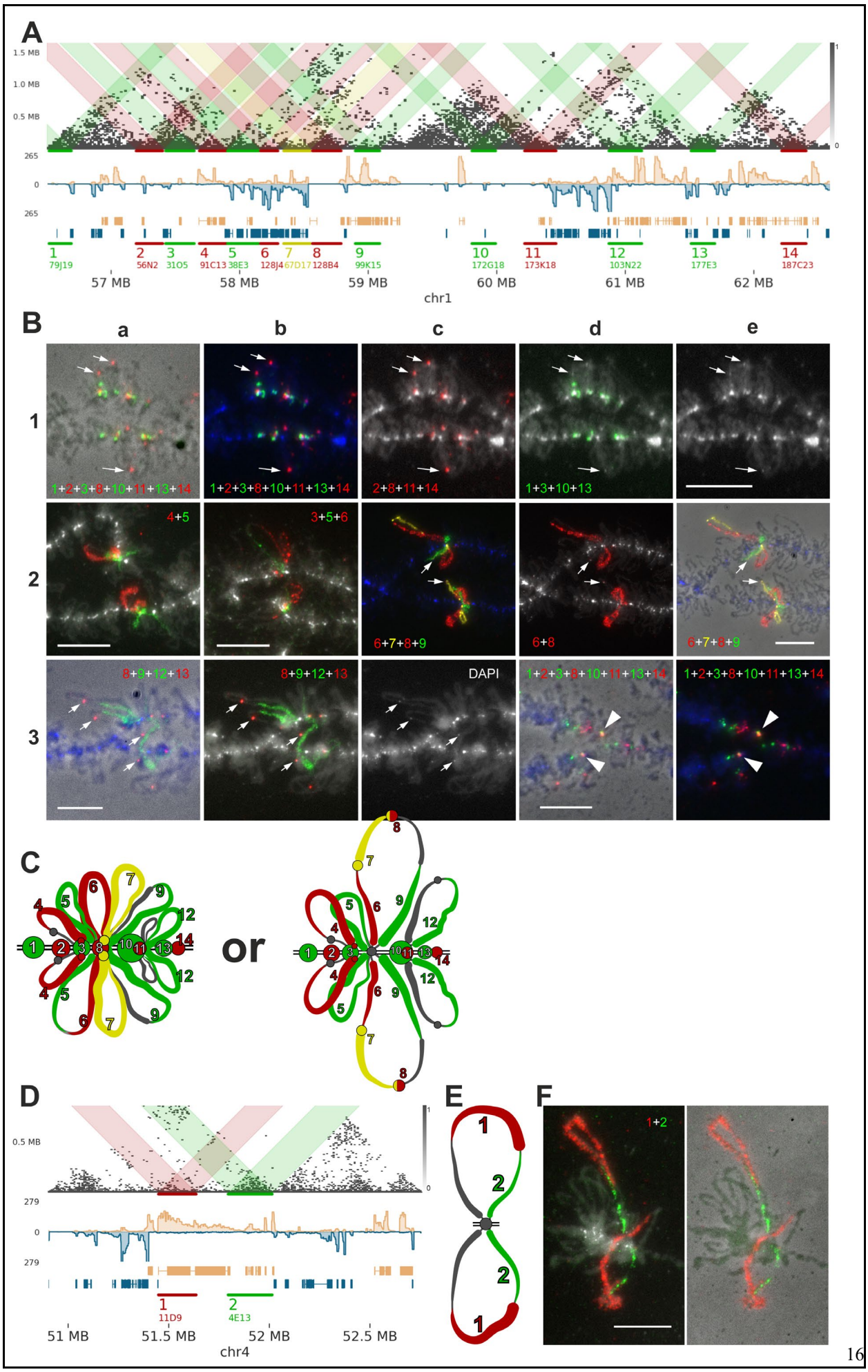
A
1.5 MB
1.0 MB
0.5 MB
265
0
265
1 79J19
2 56N2
3 31O5
4 91C13
5 38E3
6 128J4
7 67D17
8 128B4
9 99K15
10 172G18
11 173K18
12 103N22
13 177E3
14 187C23
57 MB
58 MB
59 MB
60 MB
61 MB
62 MB
chr1
B
a
b
c
d
e
1
2
3
1+2+3+8+10+11+13+14
1+2+3+8+10+11+13+14
2+8+11+14
1+3+10+13
4+5
3+5+6
6+7+8+9
6+8
6+7+8+9
8+9+12+13
8+9+12+13
DAPI
1+2+3+8+10+11+13+14
1+2+3+8+10+11+13+14
C
or
D
0.5 MB
279
0
279
1 11D9
2 4E13
51 MB
51.5 MB
52 MB
52.5 MB
chr4
E
F
1+2

Figure 5. Comparison of Hi-C map patterns with microscopically identified chromatin domains and loops in lampbrush chromosomes 1 and 4

A) Hi-C map and associated data for a fragment of chromosome 1. From top to bottom: Hi-C map of the oocyte nuclei, with colored highlights indicating interactions in regions covered by BAC clone-based probes; Total stranded RNA-seq data for lampbrush-stage oocyte nuclei ([56]); Annotation of transcription units based on *de novo* transcriptome analysis (see "Methods"); BAC clone numbers and names (see Supplementary Table S3).

B) FISH mapping images for different combinations of BAC clone-based probes on lampbrush chromosome 1. All panels except a1 include DAPI signals (blue or grayscale). Panels a1, e2, a3 and d3 merge fluorescent images with phase contrast images. White arrows in panels 1a-e and 3a-c indicate a compact chromatin domain without transcriptional activity (covered by BAC 8) that may either anchor to the chromosome axis or remain insulated from the axis forming an isolated knot. Arrowheads in panels 3d-e indicate partial colocalization of genomic regions covered by BACs 10 and 11 within a compact chromomere.

C) Schematic representation of chromomere-loop organization for a fragment of lampbrush chromosome 1, derived from FISH mapping data. Numbers correspond to the locations of BAC clone-based FISH probes aligned on chromosome 1.

D) Hi-C map for region A on chromosome 4. The data is presented similarly as in panel A above.

E) Schematic representation of chromomere-loop organization for region A on lampbrush chromosome 4, based on FISH mapping data. Numbers correspond to the locations of BAC clone-based FISH probes aligned on region A.

F) FISH mapping images for two BAC clone-based probes in region A on lampbrush chromosome 4. Fluorescent images are merged with DAPI-stained chromatin (grayscale) or phase contrast images. Scale bars: 10 μm.

Chromatin domains in lampbrush chromosomes are formed by a CTCF-independent mechanism

In the majority of vertebrate cell types, including chicken fibroblasts ([15]), TAD boundaries are demarcated by CTCF binding sites ([1,65]). The moderate conservation of CTCF binding site distribution across cell types, combined with a strong correlation between CTCF binding and TAD boundaries, allows CTCF enrichment to be detected even when comparing Hi-C maps to CTCF ChIP-seq data from different cell types ([15]).

However, in chicken oocyte nuclei, aggregation of CTCF ChIP-seq signals reveals no enrichment at contact domain boundaries (Figure 6A,C), indicating that these structures are formed through a CTCF-independent mechanism. To validate this finding and ensure the lack of CTCF enrichment is not due to cell type mismatch, we repeated the analysis using TAD boundaries from chicken embryonic fibroblasts and CTCF ChIP-seq data from liver. In this case, we observed strong CTCF enrichment at fibroblast TAD boundaries (Figure 6A,C), confirming the reliability of the approach and supporting the conclusion that chromatin domains in lampbrush chromosomes do not rely on CTCF for their formation.

To understand which chromatin architecture proteins can contribute to the formation of contact domain boundaries in oocytes, we explored the chicken oocyte nucleus transcriptome data (see "Methods"). Despite the absence of CTCF binding enrichment in the domain boundaries, in oocytes *CTCF* gene has the comparable transcript levels with fibroblasts. Genes for the other architectural proteins, such as *RAD21, STAG1*, *STAG2*

380 (cohesin) and *NCAP-H, NCAP-D2, NCAP-G, NCAP-D3, NCAP-H2, NCAP-G2*
381 (condensin) subunits also show comparable transcript levels in fibroblasts and oocytes
382 (Figure 6B, Supplementary Table S4). Consistent with this, the presence of SMC1A,
383 SMC3, Rad21, STAG1, and STAG2 on avian LBC axes in a punctate pattern has
384 previously been shown by immunostaining, with an enrichment of cohesin subunits in the
385 interchromomere regions and in chromomere cores ([68]). Among the condensin subunits,
386 XCAPD2 was found to accumulate in chromomeres of Xenopus LBCs ([69]). However, the
387 main cohesin subunits (SMC3, SMC1A) and the main condensin subunits (SMC2, SMC4)
388 have about ten times weaker transcript levels in the LBC stage oocyte (see Figure 6B,
389 Supplementary Table S4). In contrast, the meiosis specific cohesin subunit SMC1B in
390 oocytes has an almost thousand times higher level of transcripts than in fibroblasts
391 (Figure 6B, Supplementary Table S4). Thus, although components of extrusion
392 complexes are present at LBC-stage, their activity might be modulated by quantity of
393 proteins and usage of cell type specific subunits, potentially explaining why extrusion is
394 not blocked by CTCF binding sites as in typical somatic cells. Moreover, the
395 synaptonemal complex protein SYCP3 has been found at the axes of avian LBCs ([68]),
396 which may affect the formation of structural chromatin loops.

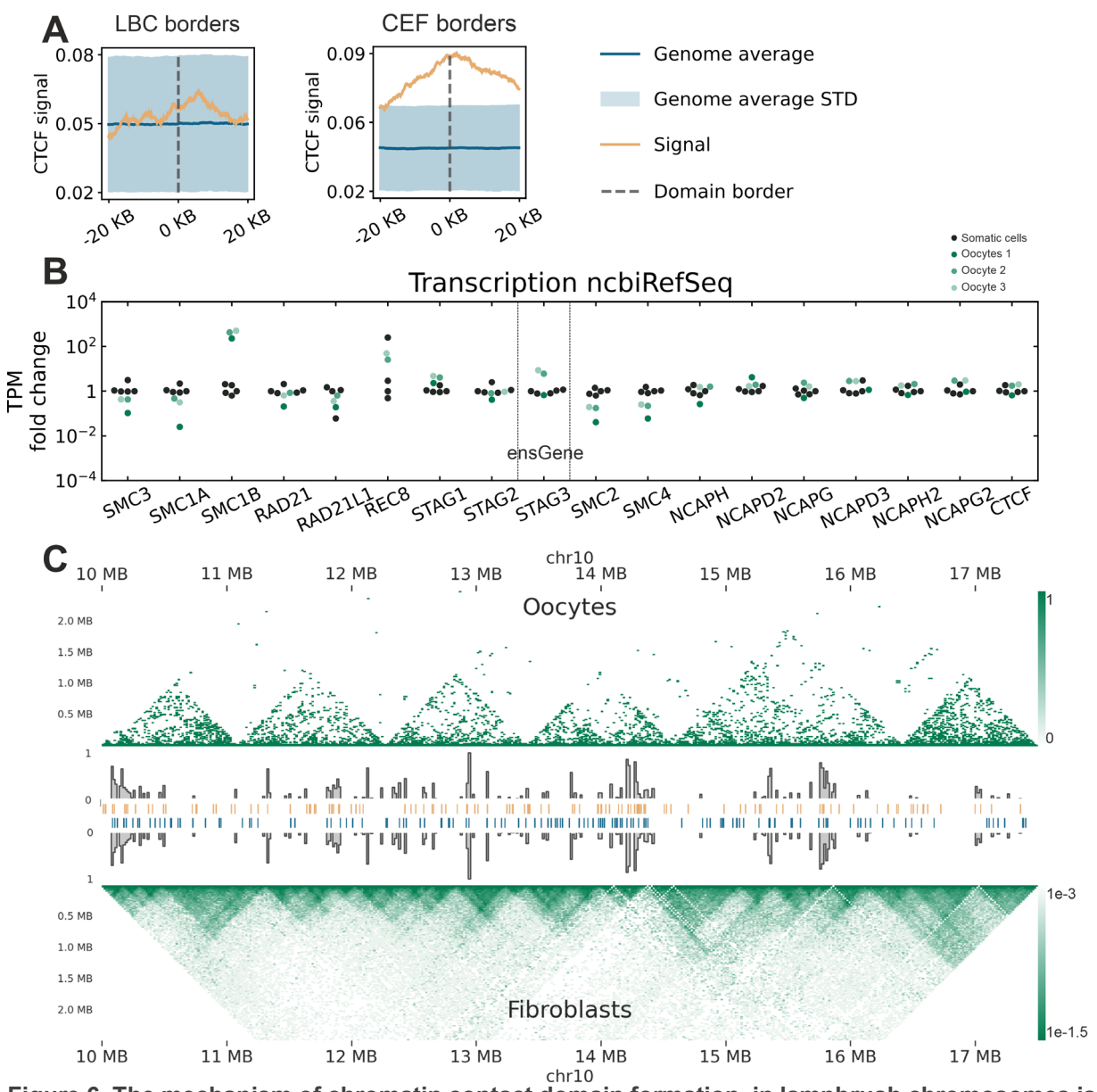

Figure 6. The mechanism of chromatin contact domain formation in lampbrush chromosomes is CTCF independent, despite transcriptional activity of the *CTCF* gene.

A) Input-normalized CTCF ChIP-seq signal from chicken liver (SRR4068194, see "Methods") at oocyte contact domain boundaries and fibroblast contact domain boundaries. The absence of CTCF enrichment across LBC domain boundaries contrasts with the strong signal observed in fibroblast boundaries.

B) Comparison of transcript levels for cohesin subunits, condensin subunits, and *CTCF* (fold-change relative to the somatic cell median expression level). Oocytes exhibit lower transcript levels for *SMC3*, *SMC1A, SMC2,* and *SMC4,* higher levels for *SMC1B* and *REC8*, but no significant difference in *CTCF* transcript levels compared to fibroblasts. Gene annotations were sourced from ncbiRefSeq, except for *STAG3*, which used ensGene annotations (see Supplementary Table S4). Green dots represent transcript levels from three chicken oocyte RNA-seq datasets, and black dots represent five replicates of chicken embryonic fibroblasts ([70]). Oocytes 1: Total RNA stranded RNA-seq data ([56]). Oocytes 2 and 3: Poly(A)-enriched stranded RNA-seq replicates generated in this study.

C) Hi-C map and CTCF distribution comparison between chicken somatic cells and oocytes. From top to bottom: Hi-C map of chicken oocyte chromatin; CTCF ChIP-seq signal from chicken liver ([71]); Forward-oriented CTCF binding sites (orange); Reverse-oriented CTCF binding sites (blue); CTCF ChIP-seq signal from chicken liver ([71]); Hi-C map of chicken embryonic fibroblasts ([15]).

397

398 *Transcriptional activity and orientation of transcription units define lampbrush*
399 *chromosome chromatin domains*

400 To investigate the genomic features underlying the formation of LBC domains, we
401 compared domain borders with position-dependent genomic elements. CpG methylation
402 levels and chromatin accessibility at domain boundaries were similar to the genomic
403 average (Supplementary Figure S7E, see "Methods"). However, boundaries showed
404 enriched GC-content relative to the background, suggesting a correlation with the
405 presence of genes.

406 Aggregation of contacts around exons, introns, and repetitive elements revealed no
407 insulatory potential for these features, arguing against their role in forming domain
408 boundaries at the lampbrush stage (Supplementary Figure S9). In contrast, we observed
409 a significant depletion of contacts across 3′-UTRs and, to a lesser extent, across 5′-UTRs
410 (Figure 7A). This suggests that the distribution and orientation of transcription units may
411 play a key role in LBC domain formation.

412 To explore the potential link between transcription and LBC domain boundaries, we
413 aligned RNA-seq data from poly(A)-enriched and total stranded RNA libraries ([56]) with Hi-
414 C maps and visually inspected these profiles. This analysis highlighted transcriptional
415 activity as a critical determinant of LBC chromatin domain organization.

416 Visual comparison of transcriptomic data with chromatin domain boundaries revealed
417 multiple transcription units absent from the current gene annotations in [[72]]
418 (Supplementary Figure S14). This discrepancy reflects the dependence of chicken
419 genome annotation on cell type and database, particularly for non-coding RNAs [[73]]. To
420 address this, we performed *de novo* transcriptome assembly using oocyte RNA-seq data,
421 generating a refined set of transcription units (TUs) active during the LBC stage (see
422 "Methods").

423 Analysis of this updated TU set confirmed a strong correlation between chromatin
424 insulation and TU orientation (Figure 7D). Genomic regions flanked by TUs in a
425 convergent (Forward-Reverse, FR) orientation exhibited the highest insulation scores
426 compared to other TU pair orientations. Furthermore, FR-oriented TU pairs were
427 significantly enriched at chromatin domain boundaries (Figure 7B).

428 Manual validation of domain boundaries revealed that nearly half of non-FR TU pairs
429 initially identified at domain boundaries were artifacts of automatic domain annotation or
430 transcriptome assembly (26 of 47 randomly selected for inspection boundaries;
431 Supplementary Figure S15). Overall, convergent transcription accounts for at least 79%
432 of domain boundaries, with 62% supported by automatic annotation and an additional
433 17% identified through manual correction.

434 Given the central role of transcription in defining LBC chromatin domains, we designate
435 the domains detected in Hi-C maps as **T**ranscription-**D**ependent **D**omains (**TDDs**).

436 Although the majority of TDD boundaries are formed by TU pairs in a convergent (FR)
437 orientation, only ~15% (~20% after manual curation) of FR-oriented TU pairs create

boundaries, while the remainder are located within domains (Figure 7C). To investigate the properties of TU pairs associated with boundary formation, we compared transcript features of "border" versus "non-border" TU pairs in a convergent orientation (Figure 7E). No single feature was sufficient to distinguish "border" TU pairs from "non-border" pairs. However, we observed that TU pairs forming boundaries tend to have several distinguishing characteristics: they are, on average, longer, separated by a larger intergenic interval, and exhibit higher activity of the weaker TU of the pair. The activity of the stronger TU in the pair shows minimal difference between boundary-forming and non-boundary-forming pairs. These observations suggest that TDD boundary formation is governed by a complex interaction of TU features rather than a single determinant.

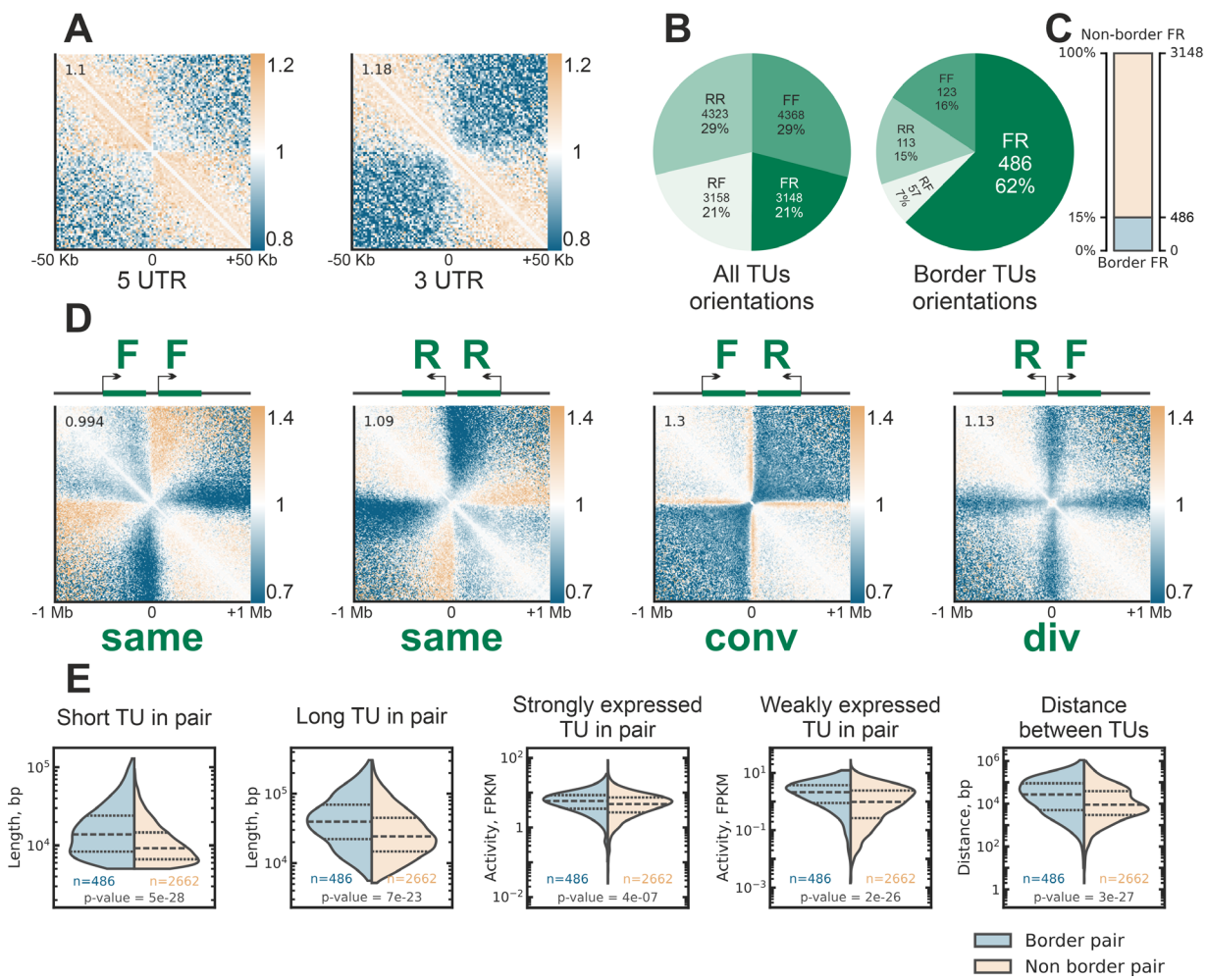

Figure 7. Aggregated 3D chromatin interaction profiles reveal genomic features underlying lampbrush chromosome chromatin domains

A) Aggregated contact maps around 5′ and 3′ UTRs show depletion of interactions across these regions.

B) Pie charts displaying transcription unit (TU) orientations for all TU pairs and those forming domain boundaries. A significant enrichment of Forward-Reverse (FR, convergent) orientation is observed at domain boundaries.

C) Statistics of FR-oriented TU pairs. Despite their prevalence at domain boundaries, only ~15-20% of FR-oriented TU pairs form boundaries.

D) Aggregated contact maps centered between TUs in different orientations: Forward-Forward (FF, co-directional), Reverse-Reverse (RR, co-directional), Forward-Reverse (FR, convergent) and Reverse-Forward (RF, divergent). Insulation score, shown in the upper-left corner of each map, is highest for

convergent (FR) TU pairs. RF pairs typically form a "cross" pattern, while FR, FF, and RR pairs display a stripe-like enrichment of contacts between TUs and upstream loci, with FF and RR stripes widening with distance from the diagonal.
E) Comparison of TU features between border-forming and non-border FR-oriented TUs. Border-forming TUs are, on average, longer, more highly expressed, and separated by greater intergenic distances. However, the length of the shorter TU and the activity of the weaker TU in the pair are more predictive of boundary formation than the features of the longer or more strongly expressed TU.

449

450 *Interplay between chromatin extruders and RNA-polymerase complex explains formation*
451 *of transcription-dependent domains in lampbrush chromosomes*

452 The presence of cohesin and condensin subunits on LBCs, combined with the enrichment
453 of TDD boundaries with convergent transcription units, lead us to the hypothesis that
454 interactions between chromatin extrusion complexes and RNA polymerase II drive LBC
455 domain formation. This model, previously proposed in the context of bacterial
456 chromosomes ([34,74]) and mouse chromosomes under Wapl/CTCF-depleted conditions
457 ([36]), suggests that RNA polymerase acts as a steric barrier for extruders.

458 Inspired by the RNA polymerase-extruders interaction model described in ([36]), we
459 developed a coarse-grained model of LBC chromatin as beads-on-string, incorporating
460 key adaptations to reflect unique LBC features (see “Methods”): 1) we connected two
461 sister chromatids by passive cohesive cohesin, representing cohesin without extrusion
462 activity; 2) DNA segments encoding actively transcribed genes are modeled with reduced
463 linear compaction, reflecting their nucleosome-free state; 3) Locus-specific RNA
464 polymerase density is incorporated based on observed TU FPKM values; 4) Bead sizes
465 were adjusted, using the polymer model from ([75]), to account for the volume of
466 ribonucleoprotein complexes associated with transcription; and 5) A simple square-
467 distance repulsion force was applied to beads to simulate chromatin interactions. These
468 modifications allow the model to capture critical features of transcription-driven LBC
469 organization.

470 We compared modeled and observed contact maps for single transcription units, stratified
471 by gene length and expression levels. Aggregated Hi-C maps for long transcribed genes
472 show insulatory boundaries at the 5′ UTR and a distinctive “cross-like” pattern formed by
473 the TU body (Figure 8A). Our model successfully reproduces these patterns (Figure 8A).

474 While insulation caused by actively transcribed genes has been previously reported and
475 modeled ([36]), prior studies did not observe the “cross-like” pattern centered around
476 individual genes. We propose that this pattern arises from two factors: nucleosome
477 removal and ribonucleoprotein matrix repulsion. Nucleosome removal linearly elongates
478 the chromatin segment, while the RNP matrix repulsion spatially separates the active
479 transcription loop from other chromatin regions. Even when a small part of the TU loop is
480 attracted to the chromomere by loop-extruding factors (LEFs), the majority of the TU loop
481 DNA remains separated from the chromomere due to RNP matrix repulsion. This
482 mechanism effectively explains the observed “cross-like” patterns.

In addition to nucleosome removal and RNP matrix repulsion, our model incorporates modulation of LEFs speed due to interactions with RNA polymerase. This property makes TUs asymmetric, directionally permeable — that is, permeable in only one direction — barriers for extrusion complexes and gives rise to distinct chromatin interaction patterns for convergent, divergent, and co-directional TU pairs.

For example, in the case of convergent TU pairs, the extruder's "legs" are effectively "locked" between the TUs (Figure 8D,E), resulting in chromatin between the TUs predominantly interacting with itself. Furthermore, loci upstream and downstream of the convergent TU pair are isolated from each other, as one of the extruder's "legs" becomes "locked" upon encountering a TU. This mechanism provides a robust explanation for the characteristic insulation and interaction patterns observed in convergent TU pairs.

To validate the hypothesis that LEF speed decreases due to interactions with RNA polymerase, we compared Hi-C data across different TU pair orientations with predictions from our model (Figure 8B). For convergent TU pairs, the model accurately reproduces the stripe pattern observed at domain boundaries and matches the experimental insulation score. The model also explains why the activity of the weaker TU in a pair is the most critical feature: if the weaker TU is sufficiently active to act as a directional barrier, the pair can halt the extruder's "leg" and enforce insulation.

The "cross-like" pattern characteristic of divergent TU pairs is also captured by the model, albeit less prominently, and the model correctly reflects the lower insulation score of divergent TUs compared to convergent TUs (1.17 for divergent vs. 1.33 for convergent). As noted earlier, the stripe for co-directional TUs becomes thicker with increasing distance from the diagonal, and this feature is partially reproduced by the model. The insulation score for modeled co-directional TU pairs is unexpectedly higher than that for modeled convergent TU pairs at a resolution of 5 Kb (1.48 vs. 1.33, respectively; Figure 8B), although it is lower for other resolutions (Supplementary Figure S10B).

Overall, these results confirm that the model accurately reproduces the distinct interaction patterns of transcription unit pairs observed in Hi-C data. We conclude that only the convergent (FR) orientation of TUs can generate the strong insulation characteristic of transcription-dependent chromatin contact domains. This is because the FR orientation "locks" one or both extruder "legs" between the TUs, effectively insulating upstream chromatin from downstream regions. Other TU pair orientations can also produce insulation-like patterns on Hi-C maps, but only under specific conditions. For example, multiple long, highly active genes in close proximity (e.g., FFFFFFFF for co-directional or RRRRFFFF for divergent orientations) can create an apparent insulation pattern. However, this effect arises primarily from the overlapping "cross-like" patterns generated by the long region of active transcription, rather than direct insulation by TU pairs.

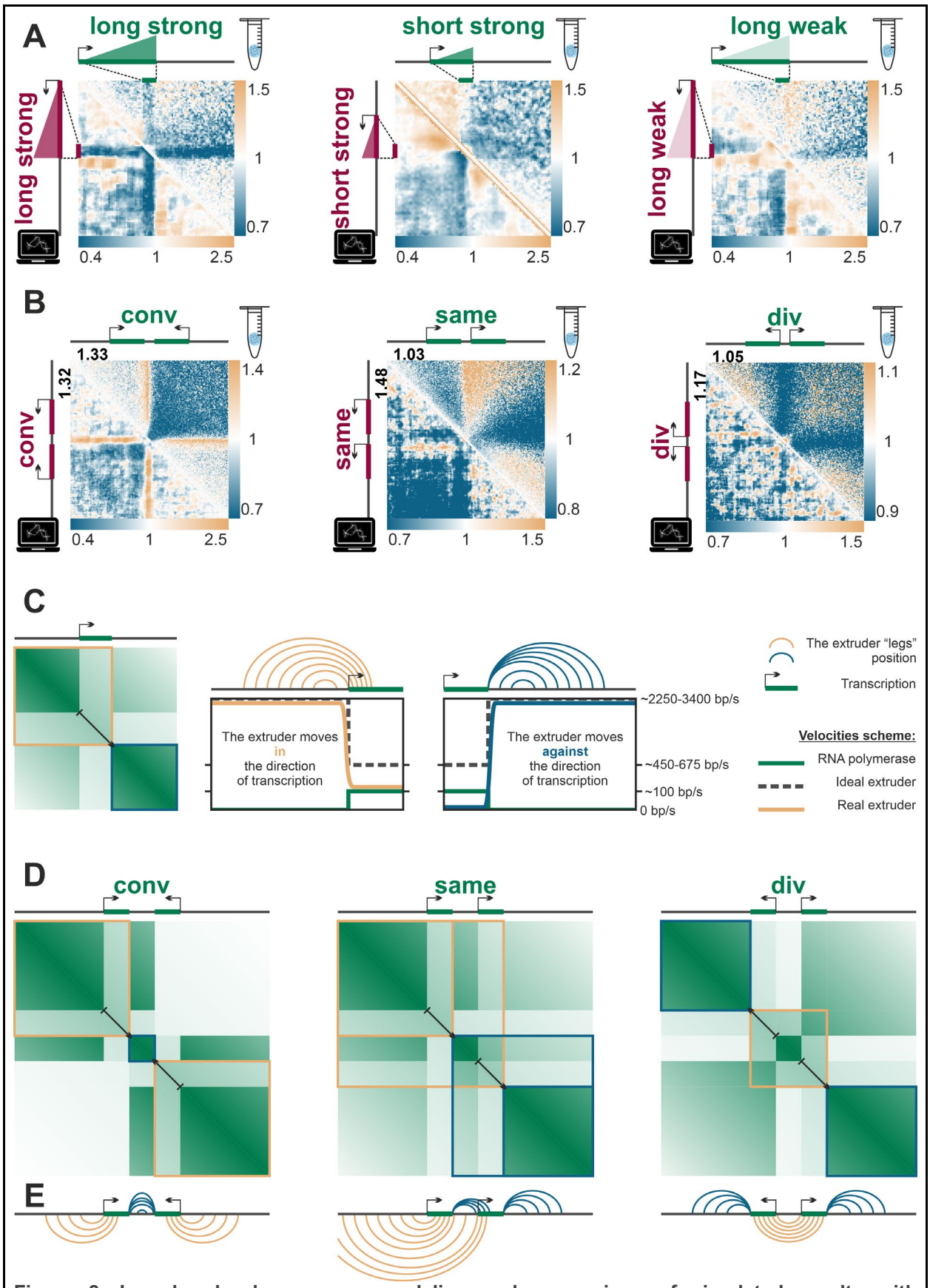

Figure 8. Lampbrush chromosome modeling and comparison of simulated results with experimental data

A) Aggregated contact maps for single transcription units (TUs). All TUs were rescaled to occupy 1/12 of the figure width, supplemented with a window of ±6 TU lengths around the TU end.

B) Aggregated contact maps centered on the midpoint between neighboring TUs with different orientations. A window of ±500 Kb around the midpoint was used. Insulation scores are displayed in the upper-left corner of each aggregated map triangle. For both A and B, the upper triangles represent experimental data, and the lower triangles show simulation results. The color bar values chosen for better contrasting the contact patterns.
C) Schematic representation of aggregated contact maps for a single TU, along with diagrams illustrating extruder velocities when moving "in" or "against" the transcription direction.
D) Schematic representation of aggregated contact maps centered on the midpoint between TUs with different orientations.
E) Extruders “legs” positions at different time points for each TU pair orientation

Validation of lampbrush chromosome chromatin simulations using FISH-mapping microscopy data in individual regions

To confirm that our simulations reproduce not only genome-averaged Hi-C patterns but also the 3D structures of individual loci, we simulated chromatin structures for regions on chromosome 1 previously analyzed by FISH (Figure 9A). To compare the simulation results with FISH data, chromatin segments were color-coded in grayscale based on AT-fraction (to mimic DAPI staining) or assigned pseudocolors matching BAC clone hybridization images (Figure 9B,C; Supplementary Table S3). To visualize the nascent RNA on a chromatin, we plotted each bead using bead size proportional to the model-predicted bead sizes.

We simulated lampbrush chromosome segment containing three key structural elements: condensed DNA domains located on the chromosome axis, corresponding to chromomeres; elongated transcription loops separated from the chromosome axis but anchored to chromomeres; and "bridges," decondensed chromatin collinear with the chromosome axis that connects neighboring chromomeres (Figure 4A, Figure 5B,C, Figure 9A).

Our simulations show that the chromomeres are enriched with cohesive cohesin complexes and LEFs. Loops 4 and 5 (Figure 9B), and the combination of loops 6-7-8-9 (Figure 9C) in the simulations closely resemble the structures observed in microscopy images of LBC 1. The simulations reveal that loop segments with active transcription exhibit a higher persistence length, meaning they are less bent, compared to non-transcribed segments (Figure 9B). This pattern was also evident when comparing the less actively transcribed loops 6 and 7 with the more transcriptionally active loop 9 (Figure 9C).

We propose that the increased bead size in the simulations, representing the accumulation of the RNP matrix, generates repulsion forces that reduce chromatin bending. This difference in bead size, which reflects the varying RNP amounts, appears sufficient to replicate the higher bending energy observed for long, actively transcribed TUs in lampbrush chromosomes. These findings highlight the critical role of nascent RNA in shaping transcription loops through physical repulsion.

Finally, we demonstrate that polymer models can successfully simulate the 3D structures of complete chicken chromosomes. We find that ~12 Mb chromosome segment models

exhibit a remarkable resemblance to the cytologically observed structures of lampbrush chromosome segments (see online supplementary data at https://genedev.bionet.nsc.ru/ftp/by_User/tlagunov/LBCs/htmls/). These models capture the key architectural features of LBCs, providing a robust framework for understanding their unique organization and facilitating direct comparisons with experimental data.

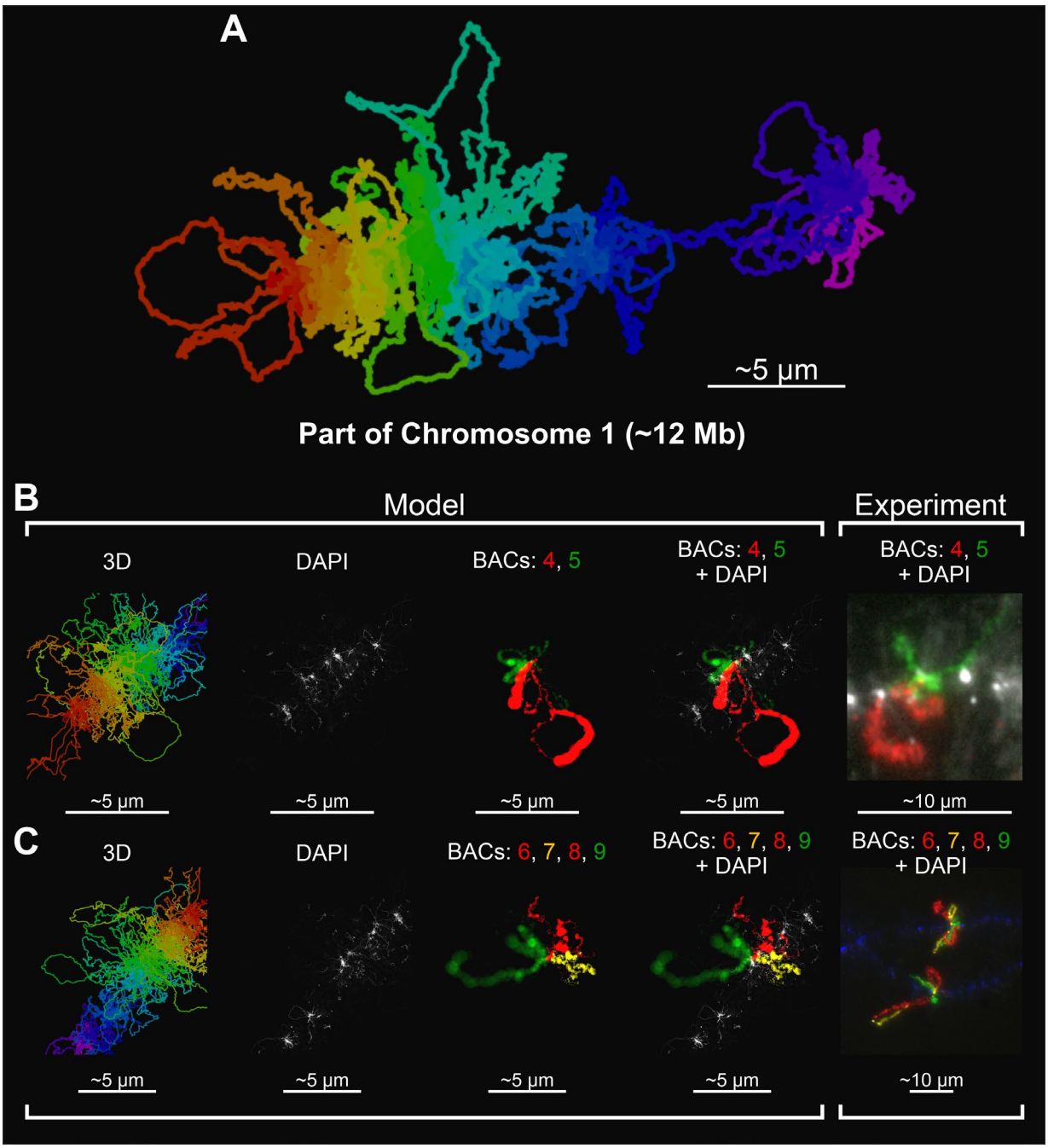

Figure 9. Comparison of lampbrush chromosome chromatin simulation with FISH-mapping microscopy images.

A) The 3D structures of the part of chromosome 1 from 53.5 Mb to 65.5 Mb.

B and C) Sets of images (left to right) showing: Modeled 3D structure with each sister chromatid painted in a rainbow gradient reflecting genomic coordinate; Modeled 3D structure painted in grayscale to reflect AT-rich chromatin; Modeled 3D structure painted in pseudocolors corresponding to BAC clone hybridization images, with bead sizes proportional to simulated bead sizes, allowing to visualize nascent RNA; Combined visualization with both grayscale (AT-fraction) and pseudocolor scales; Microscopy images of lampbrush chromosome 1 fragments showing experimental BAC clone-based probe

hybridization (for details, see also Figure 5 and Supplementary Table S3).

558

559 *Fusion of transcription-dependent domains during oocytes growth*

560 Growth of chicken oocyte coincides with reduced transcriptional activity and gradual
561 contraction of both chromosomes and lateral loops ([76]). To study the dynamics of this
562 process, we isolated nuclei from the late-diplotene stage oocytes (hereinafter referred to
563 as post-LBC) and performed a single-nucleus Hi-C experiment (Figure 1A,
564 Supplementary Table S1,2). Overall, Hi-C patterns detected in the mid-diplotene (LBC)
565 stage persist at the post-LBC stage. However, there were quantitative differences.
566 Concordant with cytological evidence of LBC contraction, we observe an increase of long-
567 range interactions at the post-LBC stage (Figure 10A,B; Supplementary Figure S7B,C).
568 Moreover, the significant decrease of the loop sizes of the chicken post-LBC
569 chromosomes ([76]) agrees well with the almost complete absence of the "cross-like"
570 patterns (Figure 10F). This observation confirms our suggestions about the critical role of
571 the TU loop repulsion in the "cross-like" pattern formation.

572 Despite the absence of "cross-like" patterns, domain patterns can be identified on the Hi-
573 C maps of late-diplotene oocytes, and the majority of the boundaries coincide with TDD
574 boundaries of LBC oocytes. However, post-LBC Hi-C maps contain fewer boundaries,
575 resulting in increase of domain lengths (Figure 10C). Visual inspection shows that about
576 half of the neighboring LBC TDDs were fused at the post-LBC stage (44 borders out of
577 97 examined on chromosome 3, Figure 10B). Genome-wide quantification shows that
578 interaction frequency between neighboring domains in post-LBC oocytes are also
579 increased (11% of contacts between domains in normal oocytes vs 22% of contacts for
580 late oocytes). Additionally, analysis of the border of TU pairs shows that the activity of
581 weakly expressed TUs decreases, as well as does the insulation (Figure 10D,E).
582 Interestingly, despite the absence of the "cross-like" pattern of actively transcribed TUs,
583 the insulation by the convergently oriented TUs is still present (Figure 10F).

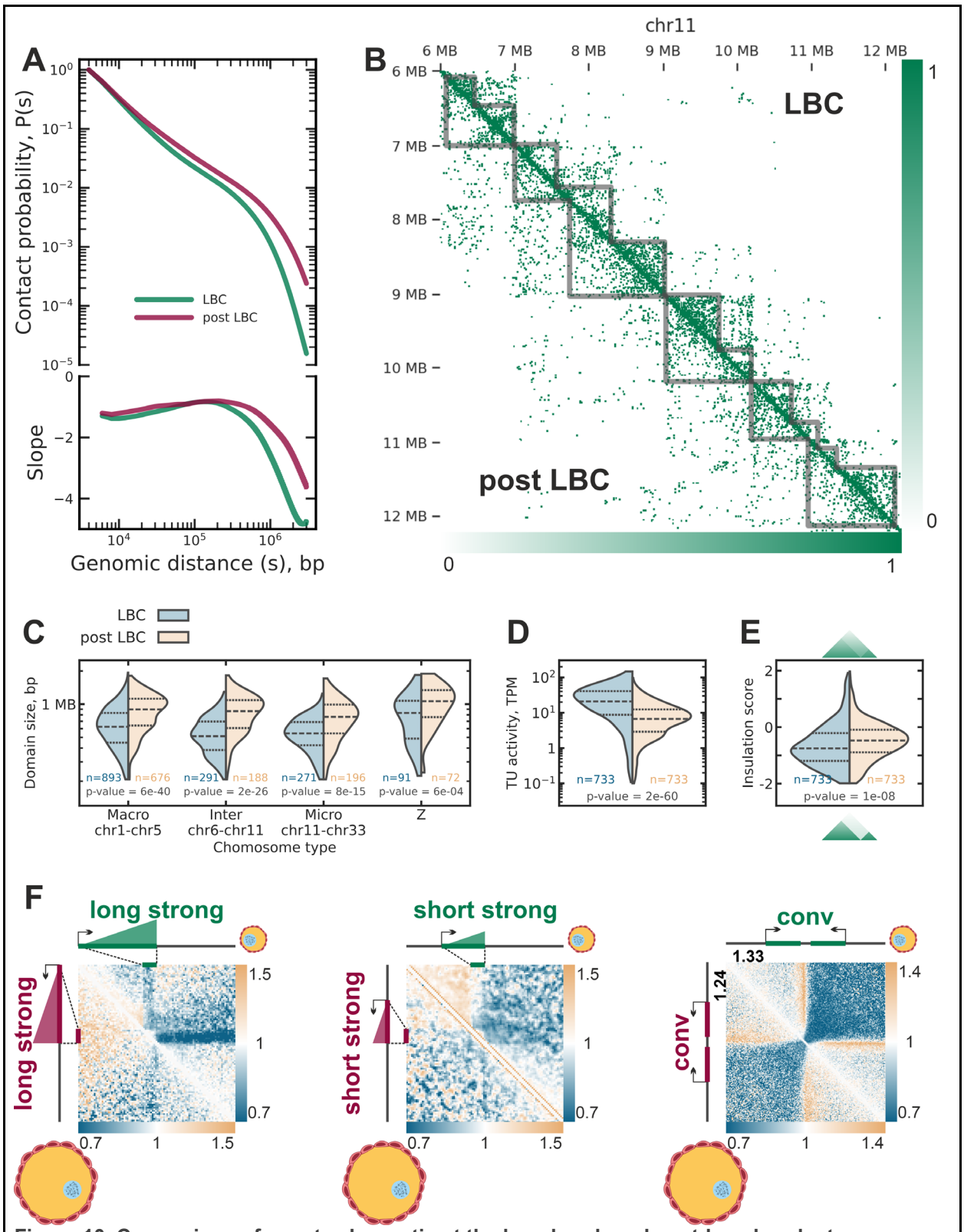

Figure 10. Comparison of oocyte chromatin at the lampbrush and post-lampbrush stages.
A) Contact probability as a function of genomic distance for lampbrush (LBC) and post-lampbrush chromosome (post-LBC) stages. Post-LBC chromatin exhibits an increase in distant contacts, consistent with microscopy observations ([76]).
B) Hi-C interaction maps for LBC and post-LBC chromatin. Grey lines indicate domain borders for each stage. Neighboring domains fuse in the post-LBC stage, as demonstrated in the shown examples.
C) Distribution of domain sizes across different chromosome types. The post-LBC stage shows an increase in mean domain size alongside a reduction in the total number of domains.
D) Transcriptional activity of TUs located at domain borders at LBC and post-LBC stages.

E) Distribution of insulation scores (see “Methods”) for domain borders at LBC and post-LBC stages. Lower scores indicate stronger insulation.
F) Aggregated Hi-C maps comparing LBC (upper triangle) and post-LBC (lower triangle) chromatin. While the "cross-like" pattern of strong single TUs diminishes significantly in the post-LBC stage, convergently oriented TUs continue to form the insulatory boundaries.

Discussion

A unified model of lampbrush chromosomes formation. Our study offers the first comprehensive, genome-wide analysis of chromatin architecture in chicken oocytes during the lampbrush chromosome stage. Rigorous statistical analysis of genomic and epigenetic datasets, along with FISH validation, underscore the high quality of the data and the robustness of our single-cell Hi-C protocol ([62]). Despite lampbrush chromosomes being discovered over a century ago ([77,78]), our findings provide a new understanding of their architecture and function at unprecedented resolution and across the entire genome. By integrating these results with established knowledge and applying polymer physics, we propose a unified model elucidating the mechanisms underlying lampbrush chromatin organization (Figure 11).

Hypertranscription is the primary driver of lampbrush chromosome formation, which determines their chromomere-loop organisation ([56]). Here we highlight several mechanisms linking transcriptional activity to their distinctive organization. Several mechanisms bridge transcriptional activity with unique features of LBC organization. First, the accumulation of ribonucleoprotein complexes along the transcription axis increases chromatin stiffness ([50,75,79]) and generates pressure that pushes transcription units outward from the chromatin axis. Second, RNA-polymerase complexes travel along a DNA template as a tightly spaced convoy, displacing DNA-bound proteins from transcription units ([80,81]). The removal of histones, combined with increased chromatin stiffness, extends the length of transcription loops.

Not all proteins, however, can be displaced by RNA polymerase. Cohesive cohesin, which topologically entraps DNA to hold sister chromatids together, most probably resists disassembly ([82]). Instead, RNA polymerase translocates SMC complexes along the DNA ([82–84]), functioning as a motor that slides cohesive cohesin toward the ends of transcription units ([82]). Similarly, cohesin with extrusion activity is translocated or disassembled during transcription ([35–37]). This creates directional barriers for the extrusion machinery at transcription unit ends, either through direct interactions with the transcription complex or indirectly via accumulated cohesive cohesin, which blocks reloading of dynamic cohesin extruders ([85]).

Active transcription zones remain free of cohesive cohesins, locally decoupling sister chromatids. In contrast, downstream regions of transcription units enriched in cohesive cohesin remain tethered to the chromosomal axis (Figure 11).

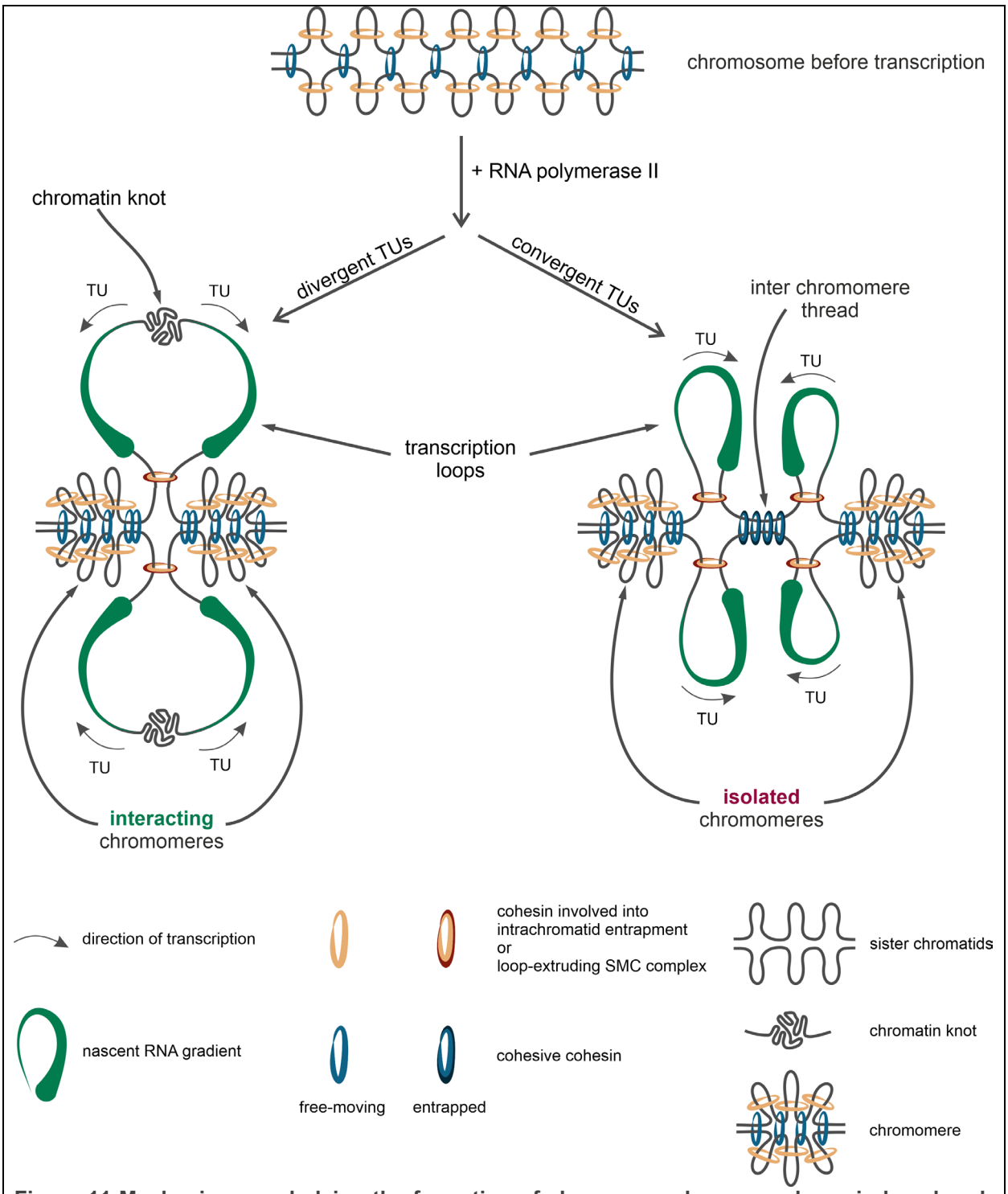

Figure 11 Mechanisms underlying the formation of chromomere-loop complexes in lampbrush chromosomes.
Active transcription increases chromatin stiffness and generates pressure that pushes transcription units (TUs) outward from the chromatin axis. Elongating RNA-polymerases remove histones and translocate cohesive cohesin towards the ends of transcription units. In the case of convergent transcribed gene pairs, this results in accumulation of cohesive cohesin complexes between transcription units, anchoring two transcription loops to the chromosomal axes. In the case of divergent transcribed gene pairs, the depletion of cohesive cohesin rings between transcription units results in the detachment of the condensed chromatin knot from the chromatin axes. Loop-extruding SMC complexes active within transcriptionally-silent regions form compact chromatin domains located on chromosomal axis. Transcriptionally-silent regions separated by divergently oriented transcription units can be bridged by extruders moving co-directionally with transcription and/or by intrachromatid entrapment by non-extruding cohesin. However, separation by convergently oriented transcription units forms impenetrable barrier for extrusion due to cohesive cohesin accumulation, precluding interactions between flanking

regions. These mechanisms underlie the segmentation of lampbrush chromosome into distinct chromomere-loop complexes.

We argue that the proposed mechanisms align closely with both cytological and molecular data, providing a comprehensive explanation for key aspects of lampbrush chromosome (LBC) organization. A defining feature of LBCs is the presence of transcription loops, both monogenic and multigenic, varying in length ([56]). Integration of Hi-C maps, oocyte nuclear RNA-seq data, and FISH mapping reveals that transcription loops often appear as Hi-C "cross" patterns, characterized by reduced contacts with adjacent regions. This pattern is consistent with loops being histone-free transcription units extruded from the chromatin axis due to ribonucleoprotein pressure, increased stiffness, and cohesive cohesin depletion (Figure 11). Furthermore, the depletion of cohesive cohesin within looping regions leads to localized decoupling of sister chromatids, a finding that correlates strongly with cytological observations.

Transcriptionally inactive regions are enriched with extrusion complexes and cohesive cohesins, leading to their compaction and appearance as contact domains with long-range interactions (Figure 11). FISH analysis shows that transcriptionally inactive regions correspond to intrachromomeric loci (this study and [[56,60]]). Combined with transcription-dependent lateral loops, these compact regions form the characteristic chromomere-loop complexes of lampbrush chromosomes ([48]). Our model of inactive chromatin organisation within chromomeres is based on previous models of lampbrush chromomere structure that involve cohesive cohesin and condensin complexes in maintaining lampbrush chromosome axes ([49,86–88]). In particular, cohesin complex subunits have been revealed within chromomere cores and in interchromomeric regions ([68]), while condensin subunit has been found to be enriched within chromomeres ([69]). Moreover, we have taken into account microscopic observations of the rosette structure of discrete lampbrush chromomeres separated by interchromomeric fibre, as well as formation of double-loop bridges upon longitudinal stretch ([47]).

Our data reveal how transcription-dependent repositioning of SMC complexes establishes boundaries between chromomere-loop complexes (Figure 11). A single transcribed gene creates a unidirectional barrier at its termination site but does not fully insulate flanking regions, as extrusion complexes can move co-directionally with transcription. Similarly, clusters of closely spaced co-directional genes result in SMC complex accumulation at the end of the last transcription unit, allowing residual interactions between adjacent regions.

In contrast, convergent gene pairs concentrate cohesive cohesin complexes between transcription units, forming an impenetrable barrier and anchoring two transcription loops to the chromosomal axis (Figure 11). Consistent with our Hi-C and cytological data, convergent gene pairs define boundaries between chromomere-loop complexes. Longer genes in a convergent pair increase the likelihood of at least one cohesive cohesin molecule being translocated to the intergenic region, reinforcing the boundary. Thus, the probability of boundary formation scales with gene length.

Unlike intergenic regions between convergent gene ends, those separating divergent gene starts are depleted of cohesive cohesin rings (Figure 11). Extrusion complexes and histones loaded within these regions mediate their compaction. The structural state of these regions depends on the presence of residual cohesive cohesin: they are tethered to the chromosomal axis if cohesin is present or remain untethered and manifest as a part of lateral loop if it is absent (Figure 11). Consistent with this, we observed small contact domains corresponding to cytologically visible chromatin knots between adjacent transcription units. These knots frequently occur when divergent genes are transcribed in opposite directions from a compact chromatin domain ([56]), aligning with the described mechanisms.

Extrusion complexes loaded between divergent gene pairs can traverse the genes co-directionally with transcription, bridging flanking regions. Thus, a divergent gene pair can form a loop without strong insulation of neighboring loci. In contrast, as discussed above, convergent gene pairs block extrusion complexes due to cohesive cohesin accumulation between them (Figure 11). This mechanism explains the observed enrichment of convergent gene pairs at contact domain boundaries.

The proposed mechanisms comprehensively explain the defining features of lampbrush chromosomes, including the formation of transcription-associated loops, local decoupling of sister chromatids in looping regions, compaction of transcriptionally inactive chromatin, and the alignment of convergent gene pairs with chromomere boundaries. Simulations based on these mechanisms using a physical chromatin model accurately reproduce both the genome-wide statistical properties of chromatin contact distribution and the specific packaging observed at individual loci.

Opened questions. Although the obtained data unequivocally shows that interaction between RNA polymerases and SMC complexes is the major mechanism explaining LBC formation, nuances of this mechanism remain to be discovered.

It is not clear how many extrusion complexes are involved in LBC organization and what is their subunit composition. It is established that the XCAPD2 (condensin I subunit) and RAD21/RAD21L (cohesin subunit) are present on the lampbrush chromosome ([68,69]). However, it remains unclear whether RAD21 functions solely within cohesive cohesin or also as a part of extrusive cohesin. This leaves the possibility of one to four types of extruders contributing, including cohesin-STAG1, cohesin-STAG2, condensin I, and condensin II, each potentially varying in lifetime, density, and velocity.

From the observed peak positions of the P(s) slope (Supplementary Figure S7A-C), we estimate an extruder density of approximately 1 per 100–200 Kb in our models. This is comparable to the density of condensin II in interphase or condensin I in prometaphase ([89]).

The question of the number of extrusion complexes involved in LBC organization can be partially addressed by analyzing constraints on loop-extruding factor lifetimes. To reproduce the frequency of distant chromatin contacts, a long LEF lifetime is required. However, longer lifetimes result in prolonged residence of extruders at the ends of actively transcribed genes, whereas shorter lifetimes allow more frequent interactions with the

gene body. This dual requirement suggests a functional specialization of extruders: long-lived extruders are necessary to establish distant chromatin contacts, while short-lived extruders facilitate interactions between the gene body and flanking chromomere regions. Based on these dynamics, we hypothesize the existence of at least two extruder types: one with a shorter lifetime to mediate gene-chromomere interactions and another with a longer lifetime to support long-range chromatin contacts. This dual mechanism could reconcile the observed patterns of chromatin organization in LBCs.

Another open question concerns the probability of an extruder traversing chromatin in the direction opposite to RNA polymerase. Banigan et al. ([36]) assumed the permeability of RNA polymerase to SMC with probability ~0.01 s^-1, but our analysis suggests that this value is too low to reproduce LBC Hi-C data. In LBCs, RNA polymerase complexes are tightly spaced ([81]). Given a polymerase velocity of ~100 bp/sec [[90]] and the extruder velocity of 675 bp/sec [[91]] results in the overstep probability of ~0.15. This oversteps probability indicates that the extruder would frequently become blocked within the gene body. Therefore, the permeability must exceed 0.15 for extruders moving against the direction of transcription to pass through the gene body effectively. This increased permeability would allow extruders to traverse tightly packed transcription units, aligning with the observed chromatin organization in LBCs.

Our model highlights the critical role of cohesive cohesin relocation in response to transcriptional activity, alongside interactions between RNA polymerase and extrusion complexes, in shaping lampbrush chromosome (LBC) architecture. Interestingly, in yeast, transcription has been shown to promote chromatin loop formation even in the absence of loop extrusion ability in the cohesin variants ([84]). The authors propose that cohesin can facilitate intrachromatid loop formation by topologically entrapping chromatin near transcription sites. Similarly, the hypertranscription characteristic of the lampbrush chromosome stage could contribute to chromatin loop formation through a transcription-dependent mechanism involving DNA loop capture by cohesin, independent of extrusion activity. This suggests that cohesive cohesins may partially supplement the role of extrusion complexes in establishing LBC architecture, emphasizing a combined mechanism of loop extrusion and transcription-dependent loop capture in shaping these remarkable chromatin structures (Figure 11).

Another unresolved question is why CTCF-mediated insulation, a hallmark of chromatin organization in typical somatic cells, does not shape LBC contact domains in oocytes of birds in contrast to mouse diplotene oocytes at the NSN (non-surrounded nucleolus) stage ([41]). Similarly, in Drosophila, there is no enrichment of dCTCF at TAD boundaries ([92]). One hypothesis is that alterations in cohesin subunit composition during LBC formation result in complexes that lack the CTCF-interacting domain. An alternative explanation is that CTCF is unable to bind active chromatin in LBCs due to the high density of RNA polymerase complexes occupying these regions. This transcription-driven exclusion could prevent CTCF from establishing its characteristic insulatory boundaries. Further investigation is required to determine the precise mechanisms underlying this phenomenon.

742 *Principles underlying lampbrush chromosome organization are universal across cell*
743 *types.* Although lampbrush chromosomes (LBCs) exhibit a unique type of chromatin
744 organization, the mechanisms underlying their structure are universal and can be
745 observed across various cell types. For instance, transcription loops formed by long,
746 highly expressed genes in somatic interphase nuclei show extensive externalization and
747 reduced cis-contacts, resembling LBC transcription loops ([79]). Similarly, loss of contacts
748 or chromatin 'melting' was observed in the case of highly expressed long neuronal genes
749 ([93]). LBC transcription loops also resemble actively transcribed genes in polytene
750 chromosomes, which appear as puffs ([52]). Hi-C maps of *Drosophila* polytene
751 chromosomes revealed absence of TADs or chromatin contact domains in the puffed
752 regions ([94]). In addition, interbands in polytene chromosomes correspond to inter-TAD
753 regions, which contain clusters of actively transcribed genes with a broad expression
754 pattern ([92]) or the promoters and 5' ends of such genes ([95,96]). Thus, loss of chromatin
755 contacts within LBC loops is a common feature of highly transcribed genes in different
756 model species and cell types.

757 Looping of actively-transcribed genes, which do not interact with neighboring
758 transcriptionally inactive chromatin but also do not form interactions with active loops from
759 other domains, resembles the local compartments reported in oocytes ([40]) and meiotic
760 sperm cells ([43]). Similar attenuation of long-range interactions within compartments has
761 also been observed in Anopheles mosquitoes ([14]). Lack of compartments was also
762 observed in the Drosophila polytene chromosomes ([94]). In all four cases, the
763 chromosomes adopt a rod-like structure, which likely explains the absence of long-range
764 homotopic interactions in these models.

765 Previous studies have demonstrated that RNA polymerase can act as a "moving barrier"
766 to extruding complexes in bacteria ([34]), yeast ([35]), slime mold *Dictyostelium discoideum*
767 ([37]) and even for vertebrate cohesin ([36]). However, in vertebrate cells, interactions
768 between cohesin and RNA polymerase generally have a minor impact on chromatin
769 architecture, becoming noticeable only in conditions that extend cohesin's extrusion
770 activity, such as Wapl+CTCF double knockout, and through extensive data aggregation
771 across the genome ([36]). In contrast, our findings suggest that extruder-polymerase
772 interactions play a significantly greater role in the organization of lampbrush
773 chromosomes, explaining the majority of short-range interactions in diplotene oocytes.
774 These results suggest that transcription-mediated repositioning of SMC complexes
775 represents an ancient, conserved mechanism shaping chromatin architecture across the
776 tree of life.

777

778 **Methods**

779 *Oocytes isolation*

780 Chicken oocytes, with diameters ranging from 1 to 2 mm as lampbrush chromosome and
781 from 4 to 7 mm as post-lampbrush chromosome stages, were dissected from the ovary
782 of healthy chicken and placed in individual drops of cooled "5:1" medium (83 mM KCl, 17
783 mM NaCl, 6.5 mM Na2HPO4, 3.5 mM KH2PO4, 1 mM MgCl2, 1 mM DTT, pH 7.2). All

784 animal experiments were approved by the bioethics committee of the Institute of Cytology
785 and Genetics SB RAS (Protocol №66, October 9th, 2020). International guidelines were
786 followed during experimental procedures ("Guide for the Care and Use of Laboratory
787 Animals" [97]). Nuclei were isolated as described earlier ([44]), washed with "5:1" medium,
788 and transferred to a dish containing 2% formaldehyde in PBS for fixation at room
789 temperature for 15 minutes. The formaldehyde was quenched by adding glycine to a final
790 concentration of 0.125 M for 15 minutes at room temperature. The integrity of the nuclei
791 was assessed using an Olympus stereomicroscope, and the Hi-C protocol was initiated
792 immediately.

793 *Hi-C libraries preparation*

794 Individual fixed nuclei were transferred to microplate wells containing 9 µL of ice-cold lysis
795 buffer (10 mM Tris-HCl pH 8.0, 10 mM NaCl, 0.2% Igepal) for 20 minutes. The nuclei
796 were then washed with NEB3.1 + 0.5% SDS and transferred to 0.2 mL PCR tubes with 3
797 µL of NEB3.1 + 0.5% SDS. 10 µL freshly prepared 1.2% Low Melting Point Agarose were
798 added to each tube under a stereomicroscope. After solidification, 10 µL of NEB3.1 +
799 0.6% SDS was added, and the samples were incubated at 37 °C for 1 hour. SDS was
800 quenched using 10 µL of 6% Triton X-100, and chromatin fragmentation was performed
801 with 25 U of *Dpn*II at 37 °C overnight.

802 The digested chromatin ends were labeled using 5 U of the Klenow fragment in the
803 presence of biotin-15-dCTP at 22 °C for 4 hours, followed by overnight ligation at 16 °C.
804 Crosslinks were reversed by incubation at 65 °C overnight, and the Low Melting Point
805 Agarose was digested with 0.4 U Agarase for 1 hour at 42 °C. The purified DNA was
806 fragmented with *Alu*I for 1 hour at 37 °C, and next-generation sequencing (NGS) libraries
807 were prepared using the KAPA HyperPrep kit with modifications. The volumes for the end
808 repair, adapter ligation, and PCR reactions were reduced by 5-fold, 5-fold, and 2-fold,
809 respectively, and adapters were diluted to 300 nM. A biotin pull-down was performed with
810 Dynabeads MyOne Streptavidin C1 beads after the adapter ligation step, followed by 25
811 cycles of PCR. Genomic libraries were sequenced using BGI DNBseq G400 machine in
812 2x150 paired-end mode.

813 *Hi-C data analysis and quality control*

814 The illumina adapters from raw sequences were cut with cutadapt ver-4.1 [98]. Data were
815 aligned with using juicer ver-1.5.6 ([99]) script against chicken telomere-to-telomere
816 genome assembly (ASM2420605v2, [72]). The read pairs without duplicates were filtered
817 by mapping quality >= 30. Quality statistics were computed using juicer output with slight
818 modifications in cis/trans ratio estimation described previously ([100]). We performed deep
819 sequencing only for samples with duplicates percentage below 30% (estimated in test run
820 with less than 200k read pairs sequenced) and fraction of intra-fragment reads
821 percentage 20%.

822 We used juicer output to generate mcool files with cooler ver-0.10.2 ([101]). Due to the low
823 number of contacts in the dataset (~500'000 per cell), we didn't use the cooler balance
824 function. Instead, we set weights for bins with zero coverage as "nan" and weights of bins
825 with non-zero coverage as 1. Aggregated plots were made with coolpuppy ver-1.1.0 ([102])

826 with “maxshift” of 2 MB and “local” flag. The P(s) curves were calculated using cooltools
827 ([103]) gaussian smooth sigma value equal to 0.1.

828 The raw reads from [[41]] were aligned against GRCm39 genome assembly and processed
829 the same way (except cooler balance was used for mcool maps). The raw reads from [[15]]
830 were aligned against ASM2420605v2 genome assembly and processed the same way
831 (except cooler balance was used for mcool maps).

832 *Domain boundaries annotation*

833 To annotate domain boundaries for both chicken oocytes, mouse oocytes and chicken
834 somatic cells the lavaburst ver-0.2.0 was used (https://github.com/nezar-compbio/lavaburst).
835 This algorithm divides the genome into domains in such a way as to maximize a global
836 domain scoring function. The algorithm gets the gamma as a hyperparameter so it needs
837 to be found. We found the value of gamma separately for each single oocyte the same
838 way as in the ([41]) article: 1) the average domain size was calculated for each gamma
839 (taking into account only domains more than 200 Kb); 2) the gamma value that makes
840 the average domain size closest to 500 Kb for mouse NSN oocytes was used. For chicken
841 oocytes the preferable average domain size was 1 Mb.

842 The domains were divided into LUDs and SSDs by N50 threshold: all domains were
843 sorted by their size and the domain size that covers the half of the summed domain length
844 was set as threshold.

845 *Insulation score*

846 Insulation function from cooltools package ver 0.5.1 [[103]] has been used for calculating
847 the Insulation scores on merged oocytes. Resolution size is 16 Kb and window size is 2
848 Mb.

849 *Chicken liver ChIP-seq data preparation*

850 The CTCF ChIP-seq data was taken from [[71]] as sequenced reads. The reads were
851 aligned at ASM2420605v2 chicken genome assembly [[72]] and bamCoverage ver-3.5.4
852 were used to get bigwig files. The ChIP signal bigwig was divided on input signal bigwig
853 for each bin and logarithm from results were taken.

854 *NOMe-seq experiments and data analysis*

855 Nuclei were isolated and washed as described above. Individual nuclei were transferred
856 immediately to 3 µL of GC Reaction Buffer (NEB) with 0.2% Igepal for 20 minutes at RT.
857 Reaction of methylation was performed in 1x GC Reaction Buffer supplemented with 160
858 µM S-adenosylmethionine with 6U GpC Methyltransferase at 37 °C 1 hour. Proteines
859 were digested by proteinase K at 65 °C for 2 hours. Libraries for whole genome bisulfite
860 sequencing were prepared using Pico Methyl-Seq Library Prep Kit (Zymo Research)
861 according to the user manual. For control experiments we also supplemented chicken
862 oocytes nuclei with human K562 cells.

863 Genomic libraries were sequenced using the BGI DNBseq G400 machine in 2x150
864 paired-end mode.

865 The illumina adapters from raw sequences were cut with cutadapt ver-4.1 [98]. To process
866 NOMe-seq reads, we used Bismark version 0.23.0 (104,105) in conjunction with Bowtie2
867 version 2.4.4 (106–109), setting the -t parameter to 10. Reads were aligned to the
868 ASM2420605v2 genome assembly (72), and any reads with MAPQ < 10 were excluded.
869 Methylation data from the aligned reads were then converted to the *.bedgraph* format
870 using the bismark-methylation-extractor.

871 The GpC methylation profile was obtained from the NOMe-seq experiment described
872 above. The CpG methylation profile was obtained from the NOMwee-seq experiment and
873 merged with the profile from the Methyl-seq experiment from (66).

874 *RNA-seq experiments and data analysis*

875 Nuclei were isolated and washed as described above. Individual nuclei were frozen
876 immediately. Total RNA was isolated from the nuclei using TRIzol reagent (ThermoFisher
877 Scientific) according to previously described protocol (56). The RNA samples were sent to
878 BGI company to generate transcriptomic libraries using experimental workflow including
879 the following steps: 1) oligoT-enrichment; 2) RNA fragmentation; 3) first-strand synthesis
880 with random primers; 4) second strand synthesis with dUTP instead of dTTP; 5) end-
881 repair, 3'-adenylation and adaptors ligation; 6) Uracil-DNA-Glycosylase treatment
882 followed by PCR amplification and circularization; 7) Sequencing on DNBSEQ in PE100
883 paired-end mode.

884 Together with poly(A)-enriched stranded RNA-seq data generated in this study, the total
885 RNA stranded RNA-seq data from [56] were used. The illumina adapters from raw
886 sequences were cut with cutadapt ver-4.1 [98]. All data were aligned with hisat2 ver-2.2.1
887 (110) on ASM2420605v2 genome assembly (72). Bam files were prepared using samtools
888 ver-1.15.1 (111) and bigwig files were made using bamCoverage ver-3.5.4
889 (https://github.com/BGI-shenzhen/BamCoverage). Each bam file was split on subfiles by
890 strand (the direction of transcription) and duplicates were marked with “samtools
891 markdup”. The unique reads were merged from all experiments (still grouped by strand)
892 and *de novo* LBC transcript structure recovery was made with stringtie ver-2.2.2 (112). The
893 forward and reverse transcription files were separately used with stringtie and called as
894 “FORW” and “REV” respectively. Maximum gap allowed between read mappings was set
895 as 300 bp; minimum assembled transcript length = 1000 bp; minimum junction coverage
896 = 5; minimum anchor length for junctions = 10 bp; minimum isoform fraction = 0.05;
897 minimum reads per bp coverage to consider for single-exon transcript = 3.5; minimum
898 reads per bp coverage to consider for multi-exon transcript = 1.2.

899 For the expression analysis, stranded RNA-seq data of the oocyte nuclei from this work
900 and [56] was compared with the RNA-seq data of the chicken embryonic fibroblasts from
901 [70]. All raw reads were aligned on GRCg6a genome assembly. The TPMCalculator ver-
902 0.0.3 was used to calculate TPM values for genes of interest for ncbiRefSeq.2020-04-01,
903 ensGene.v101 and refGene annotations (see Supplementary Table S4).

904 *FPKM calculation*

905 The FPKM value was calculated for each gene and used as a measure of transcriptional
906 activity in analysis. *FPKM_i = 10^9 * N_i / (N_0 * L_i)*, where *i* denotes the transcript
907 index, *N_i* - number of reads mapped to transcript *i*, *N_0* - total number of mapped reads,
908 *L_i* - length of transcript *i*. To estimate the amount of nascent RNA connected to the
909 elongating RNA polymerases, the values of intron FPKM and exon FPKM were calculated
910 separately for each transcription unit annotated. The minimum transcript FPKM value was
911 used for the further analysis.

912 *Mitotic metaphase chromosomes preparation*

913 Mitotic metaphase chromosomes were prepared from chicken embryonic fibroblast (CEF)
914 culture. Cell cycle was arrested by 0.1 µg/ml colcemid (Biological Industries) for 5 hours,
915 then the cells were fixed in cold 3:1 ethanol:acetic acid mixture. The CEF suspension was
916 dropped onto the slides which had been heated in a water bath to 60°C and then air dried.

917 *Lampbrush chromosomes preparation*

918 Lampbrush chromosome spreads were prepared according to a well-described
919 procedure ([113]). The experimental procedure was approved by the Ethics Committee for
920 Animal Research of St. Petersburg State University (protocol #131–04-6 dated 25 March
921 2019). Nuclei were manually isolated from oocytes (1-2 mm), one by one, using tungsten
922 needles under a stereomicroscope Leica S9D or M165C (Leica Microsystems) in the
923 isolation medium "5:1" (83 mM KCl, 17 mM NaCl, 6.5 mM Na2HPO4, 3.5 mM KH2PO4,
924 1 mM MgCl2, 1 mM dithiothreitol, pH 7.2). The isolated nuclei were then washed in the
925 hypotonic solution ("5:1" medium diluted 4 times with the addition of 0.1% formaldehyde)
926 and transferred to the isolation chamber mounted on a microscope slide and filled with
927 the hypotonic solution. Nuclear envelope was broken manually with a pair of thin tungsten
928 needles to release the nuclear content and slides were left to disperse for 15-20 minutes
929 at +4°C. Slides were then centrifuged at 1600 g for 30 minutes at +4°C in a cytology
930 centrifuge (Hettich Universal 320R), fixed in 2% formaldehyde in PBS for 30 minutes and
931 dehydrated in a series of ethanol solutions of increasing concentrations. Specimens were
932 mounted in an antifade solution containing 1 mg/ml DAPI (Sigma), 55% glycerol, 10 mM
933 Tris-HCl, 2% DABCO (Sigma) and were imaged prior to FISH procedure.

934 *Preparation of DNA-probes*

935 To obtain DNA probes for FISH mapping of the selected scHi-C chromatin domains, 29
936 BAC clones were selected: 14 BAC clones in a region (55-50 Mb) on chromosome 1; 2
937 and 7 BAC clones in two regions (50-53 Mb and 70-73 Mb) on chromosome 4,
938 respectively; and 6 BAC clones in the region 3-7 Mb of chromosome 13 from the chicken
939 BAC-library CHORI-261 (https://bacpacresources.org/chicken261.htm) (Supplementary
940 Table S3). BAC DNA was isolated from night culture by standard alkaline lysis. DNA was
941 labeled by nick-translation ([114]) with dUTP-bio (DNA-Synthesis), dUTP-dig (Jena
942 Bioscience) and dUTP-Atto637 (Jena Bioscience) using DNA polymerase I (ABclonal)
943 and DNAse I (New England BioLabs). Labeled DNA probes in various combinations (up
944 to 10 probes in a single mixture) were precipitated with salmon sperm DNA and, in case
945 of DNA probes to the region of chromosome 1, with the C0t-5 fraction of chicken genomic

946 DNA, and dissolved to final concentration of 20 ng/µl for each DNA probe in the
947 hybridization buffer containing 50% formamide, 10% dextran sulfate and 2×SSC.

948 *Fluorescent in situ hybridization*

949 Chromosomal position of each BAC clone-based DNA probe was first verified by
950 DNA/DNA FISH on CEF metaphase chromosomes: preparations were pretreated with
951 RNAse A (Thermo Scientific) and pepsin (Sigma-Aldrich). For lampbrush chromosomes,
952 the DNA/DNA+RNA FISH procedure was used, omitting RNAse treatment ([55,115]).
953 Chromosome preparations were denatured in 70% formamide in 2×SSC at 70°C for 10
954 minutes, and dehydrated in a series of cold (-20°C) ethanol solutions of increasing
955 concentration. Hybridization mixtures were denatured at 90°C and cooled on ice and
956 applied to the slides with the denatured chromosomes. Hybridization was carried out
957 overnight in a humidity chamber at 37°C, followed by a post-hybridization wash in
958 0.2×SSC at 60°C. Biotin was detected with Alexa488-conjugated streptavidin (Jackson
959 ImmunoResearch Laboratories) and biotinylated anti-streptavidin antibody (Vectorlabs),
960 and digoxigenin was detected with Cy3-conjugated mouse anti-digoxigenin antibody
961 (Invitrogen) and Cy3-conjugated anti-mouse IgG (Jackson ImmunoResearch
962 Laboratories).

963 *Immunostaining*

964 Lampbrush chromosome preparations were immunostained with mouse monoclonal
965 antibodies against phosphorylated serine 5 of CTD repeat YSPTSPS of RNA polymerase
966 II [H14] (Abcam, ab24759), followed by the detection with Alexa-488-conjugated goat
967 anti-mouse IgG (Molecular Probes). Immunofluorescence staining procedure was
968 described previously ([68,116]).

969 *Microscopy and image processing*

970 Chromosome preparations were analyzed with the fluorescence microscope Leica
971 DM4000 (Leica Microsystems, GmbH) equipped with a monochrome CCD camera (1,3
972 Mp) and corresponding fluorescence filter cubes. LAS AF software (Leica Microsystems,
973 GmbH) was used for image acquisition, and Adobe Photoshop CS2 (Adobe) and ImageJ
974 (http://rsbweb.nih.gov/ij/) was used for image processing and layout. Schematic drawings
975 were created in CorelDRAW X5 and represent an approximation of the FISH mapping of
976 DNA probes to lampbrush chromatin domains seen in at least 4 micrographs for each
977 DNA probe.

978 *Polymer Modelling*

979 We used polymer modeling based on the Polychrom tool [[117]] to gain insights into the
980 roles of individual RNA polymerases in the folding of lampbrush chromosomes. The
981 simulation was performed in the coarse-grained model approximation, where clusters of
982 nucleosomes and individual polymerases acted as beads.

983 1D

984 The modeled object is a one-dimensional array of N beads of sizes ranging from 45 to
985 225 bp, with dynamically loaded-unloaded RNA polymerases and active extruders (loop
986 extrusion factors, LEFs) and non-removable cohesins without the loop extruding activity
987 (loaded with the density of 45 Kb).

988 The number of base pairs in a bead differs for TUs where RNA polymerases are located
989 and for transcriptionally inactive regions with a dense fit of nucleosomes. The size of 45
990 bp per bead was used to represent one RNA polymerase (~15 nm, [118]). The regions
991 between the TUs are condensed by the nucleosomes ~5 times (because ~140 bp
992 entangle it and ~70 bp are between nucleosomes). Our estimation is also close to the
993 estimation from [79]. Transcription units are placed according to the annotation obtained
994 from RNA-seq data.

995 RNA polymerases are represented as objects with the following properties: they are
996 loaded at the beginning of TUs with a probability proportional to the activity of the TU
997 (estimated from FPKM metric), from where they begin movement at a speed of vp = 100
998 bp/sec [90] (the speed of LEFs is vL = 625 bp/sec for the naked DNA [91]) along the
999 transcript. Nascent RNA fiber growth from each RNA polymerase at length *vp*dt* for the
1000 time step of *dt* seconds. The introns are excised from the pre-mRNA attached to the RNA
1001 polymerases. If the bead in the direction of movement is occupied by a LEF or cohesive
1002 cohesin (i.e. SMC), then RNA polymerase pushes the SMC [36] and all subsequent SMCs
1003 in the direction of movement until they collide with another RNA polymerase.

1004 The mechanism of LEF action is as follows. It is randomly loaded onto a pair of adjacent
1005 beads that are not occupied by another LEF or RNA polymerase. Each time one of the
1006 two LEF retaining components can reattach to the next bead in the corresponding
1007 direction releasing the occupied one. The direction of movement changes every timestep
1008 (effectively two-way movement). Each part of the LEF can move independently of the
1009 other. If the next bead is occupied by another LEF then no movement occurs. If the next
1010 bead is occupied by RNA polymerase then the LEF can bypass the RNA polymerase with
1011 the stable probability *Pbypass*. The cohesive cohesin can be pushed by LEF if the next
1012 bead is not occupied. Extruding continues until the LEF is removed from the chromatin.
1013 The probability of removal is (*1 / lifetime)* for each timestep.

1014 Some parameters for these LEFs were determined by using P(s) data from the
1015 experiment Hi-C data on lampbrush-stage oocyte nuclei (see "Supplementary methods
1016 1. Modeling"): *lifetime* = 1 Mb (~60% of LEFs will pass this distance on naked DNA),
1017 *average_loop_size* = 90 Kb (determines the density of loaded condensins on chromatin),
1018 *Pbypass* = 0.01 (as in [36] article).

1019 <u>3D</u>

1020 The next step after forming 1D snapshots of the SMCs and RNA polymerase locations
1021 on the chromatin is to transfer the interactions into 3D. For this purpose all beads are
1022 grouped into bead clusters of 10 which include nucleosomes and transcription units. The
1023 sizes of the clusters vary from 450 to 2250 bp. New beads are placed into the starting
1024 conformation form of two parallel 2D fractals, corresponding to the two sister chromatids.

1025 The distances between beads in 3D varied according to the fractal dimension of the site
1026 ("Supplementary methods 1. Modeling").

1027 With the launch of a three-dimensional simulation, at each moment in time, a spring of a
1028 fixed size (~40 nm [119]) is stretched between each pair of beads connected by a given
1029 LEF, and the beads move according to a random Brownian motion.

1030 RNA tails from 1D simulation are converted into increased bead sizes by the Marco and
1031 Siggia model [75]. The repulsive potential between beads is realized as *0.5*k*(r1+r2)^2*.
1032 A more detailed analysis of the model and parameters used is presented in the
1033 "Supplementary methods 1. Modeling".

1034 In order to reproduce the patterns observed in LBC under microscopy, the original three-
1035 dimensional regions of the chromosome were flattened to 1 μm (see "Supplementary
1036 methods 1. Modeling").

1037 Online supplementary files can be found via links (3D structure and Flattened structure)
1038 or be downloaded from git (https://github.com/genomech/LBC_model).

1039 Simulated Hi-C

1040 The resulting 3D polymers were used to construct contact maps similar to Hi-C maps.
1041 The beads of different sizes are correctly converted to Kb resolution that allow us to
1042 compare simulated and experimental contact maps of the specific chromatin slices. Since
1043 the contact map collected from one polymer conformation is essentially one conformation
1044 of an oocyte, the sum of contacts from one "*Dpn*II site" in a bead was normalized to 8 as
1045 in the experiment (see "Supplementary methods 1. Modeling" for the details). Simulated
1046 Hi-C maps were then stored in mcool format and the analyses that are the same with
1047 experiment Hi-C maps were performed.

1048

1049 **Data access**

1050 All sequencing data are available under NCBI accession PRJNA1211889.

1051 The program code used for lampbrush chromosome model simulation is freely and
1052 publicly available at https://github.com/genomech/LBC_model.

1053

1054 **Acknowledgments**

1055 This manuscript is dedicated to the memory of Joseph G. Gall. This study was initiated
1056 with support of RSF Project №20-64-46021 in 2020-2022. We acknowledge the collective
1057 centers of Ministry of Science and Higher Education of the Russian Federation (state
1058 project FWNR-2022-0019) for providing facilities for LBC isolation and genomic libraries
1059 preparation and sequencing. Access to computational resources was provided by
1060 Novosibirsk State University, supported by the Ministry of Education and Science of the
1061 Russian Federation (FSUS-2024-0018). Microscopy analysis was performed using the

equipment of the Resource Center ‘Molecular and Cell Technologies’ (Saint-Petersburg State University). Part of the bioinformatic analysis and manuscript preparation was supported by grant of the state program of the “Sirius” Federal Territory “Scientific and technological development of the “Sirius” Federal Territory” (agreement №26-03, 27/09/2024). The original manuscript text was composed by authors; proofreading was conducted with the assistance of ChatGPT version 4, after that the text was corrected and edited by the authors.

Author contributions

V.F. and A.K. conceptualized the study. M.G. conducted the genomics experiments with assistance from A.K., T.K., and A.M., who contributed to oocyte isolation, and A.N., who provided support for staining and NOMe-seq experiments. Cytological analyses, including FISH-mapping experiments, were performed by T.K. and A.K. with contribution from A.M., who performed probe labeling. Bioinformatic analyses were carried out by T.L., with contributions from V.F., A.P., A.N., and V.K. T.L. developed the methodology for polymer simulations and conducted the modeling experiments with input from V.K. T.L. and V.F. drafted the manuscript with contributions by A.K.; authors jointly developed mechanism explaining lampbrush chromosome organization, and A.K. suggested the final scheme of chromomere-loop complex formation. All authors reviewed, revised, and approved the final manuscript.

Bibliography

1. Kabirova, E. *et al.* Function and evolution of the loop extrusion machinery in animals. *IJMS* **24**, 5017 (2023).
2. Misteli, T. The self-organizing genome: principles of genome architecture and function. *Cell* **183**, 28–45 (2020).
3. 4D Nucleome Consortium *et al.* An integrated view of the structure and function of the human 4D nucleome. Preprint at https://doi.org/10.1101/2024.09.17.613111 (2024).
4. Kabirova, E. *et al.* TAD border deletion at the Kit locus causes tissue-specific ectopic activation of a neighboring gene. *Nat Commun* **15**, 4521 (2024).
5. Salnikov, P. *et al.* Structural variants in the Epb41l4a locus: TAD disruption and Nrep gene misregulation as hypothetical drivers of neurodevelopmental outcomes. *Sci Rep* **14**, 5288 (2024).
6. Rajderkar, S. *et al.* Topologically associating domain boundaries are required for normal genome function. *Commun Biol* **6**, 435 (2023).
7. Lupiáñez, D. G. *et al.* Disruptions of Topological Chromatin Domains Cause Pathogenic Rewiring of Gene-Enhancer Interactions. *Cell* **161**, 1012–1025 (2015).
8. Pope, B. D. *et al.* Topologically associating domains are stable units of replication-timing regulation. *Nature* **515**, 402–405 (2014).
9. Klein, K. N. *et al.* Replication timing maintains the global epigenetic state in human cells. *Science* **372**, 371–378 (2021).
10. Moindrot, B. *et al.* 3D chromatin conformation correlates with replication timing and is conserved in resting cells. *Nucleic Acids Research* **40**, 9470–9481 (2012).
11. Piazza, A. *et al.* Cohesin regulates homology search during recombinational DNA repair. *Nat Cell Biol* **23**, 1176–1186 (2021).
12. Strom, A. R. *et al.* HP1α is a chromatin crosslinker that controls nuclear and mitotic chromosome mechanics. *eLife* **10**, e63972 (2021).
13. Uhler, C. & Shivashankar, G. V. Regulation of genome organization and gene expression by nuclear mechanotransduction. *Nat Rev Mol Cell Biol* **18**, 717–727 (2017).
14. Lukyanchikova, V. *et al.* Anopheles mosquitoes reveal new principles of 3D genome organization in insects. *Nat Commun* **13**, 1960 (2022).

15. Fishman, V. *et al.* 3D organization of chicken genome demonstrates evolutionary conservation of topologically associated domains and highlights unique architecture of erythrocytes' chromatin. *Nucleic Acids Research* **47**, 648–665 (2019).
16. Krefting, J., Andrade-Navarro, M. A. & Ibn-Salem, J. Evolutionary stability of topologically associating domains is associated with conserved gene regulation. *BMC Biol* **16**, 87 (2018).
17. Hoencamp, C. *et al.* 3D genomics across the tree of life reveals condensin II as a determinant of architecture type. *Science* **372**, 984–989 (2021).
18. Mirny, L. A. The fractal globule as a model of chromatin architecture in the cell. *Chromosome Res* **19**, 37–51 (2011).
19. Razin, S. V. & Gavrilov, A. A. The role of liquid–liquid phase separation in the compartmentalization of cell nucleus and spatial genome organization. *Biochemistry Moscow* **85**, 643–650 (2020).
20. Rada-Iglesias, A., Grosveld, F. G. & Papantonis, A. Forces driving the three-dimensional folding of eukaryotic genomes. *Molecular Systems Biology* **14**, e8214 (2018).
21. Strom, A. R. & Brangwynne, C. P. The liquid nucleome – phase transitions in the nucleus at a glance. *Journal of Cell Science* **132**, jcs235093 (2019).
22. Cremer, T. *et al.* The Interchromatin Compartment Participates in the Structural and Functional Organization of the Cell Nucleus. *BioEssays* **42**, 1900132 (2020).
23. Li, H., Playter, C., Das, P. & McCord, R. P. Chromosome compartmentalization: causes, changes, consequences, and conundrums. *Trends in Cell Biology* **34**, 707–727 (2024).
24. Padeken, J. & Heun, P. Nucleolus and nuclear periphery: Velcro for heterochromatin. *Current Opinion in Cell Biology* **28**, 54–60 (2014).
25. Quinodoz, S. A. *et al.* Higher-Order Inter-chromosomal Hubs Shape 3D Genome Organization in the Nucleus. *Cell* **174**, 744-757.e24 (2018).
26. Solovei, I., Thanisch, K. & Feodorova, Y. How to rule the nucleus: divide et impera. *Current Opinion in Cell Biology* **40**, 47–59 (2016).
27. Dekker, J. & Mirny, L. A. The chromosome folding problem and how cells solve it. *Cell* **187**, 6424–6450 (2024).
28. Davidson, I. F. & Peters, J.-M. Genome folding through loop extrusion by SMC complexes. *Nat Rev Mol Cell Biol* **22**, 445–464 (2021).
29. Szabo, Q., Bantignies, F. & Cavalli, G. Principles of genome folding into topologically associating domains. *Sci. Adv.* **5**, eaaw1668 (2019).
30. Wang, J. *et al.* Manipulation of TAD reorganization by chemical-dependent genome linking. *STAR Protocols* **2**, 100799 (2021).
31. Dixon, J. R. *et al.* Topological domains in mammalian genomes identified by analysis of chromatin interactions. *Nature* **485**, 376–380 (2012).
32. Nora, E. P. *et al.* Spatial partitioning of the regulatory landscape of the X-inactivation centre. *Nature* **485**, 381–385 (2012).
33. Dequeker, B. J. H. *et al.* MCM complexes are barriers that restrict cohesin-mediated loop extrusion. *Nature* **606**, 197–203 (2022).
34. Brandão, H. B. *et al.* RNA polymerases as moving barriers to condensin loop extrusion. *Proc. Natl. Acad. Sci. U.S.A.* **116**, 20489–20499 (2019).
35. Rivosecchi, J. *et al.* RNA polymerase backtracking results in the accumulation of fission yeast condensin at active genes. *Life Sci. Alliance* **4**, e202101046 (2021).
36. Banigan, E. J. *et al.* Transcription shapes 3D chromatin organization by interacting with loop extrusion. *Proc. Natl. Acad. Sci. U.S.A.* **120**, e2210480120 (2023).
37. Zhegalova, I. V. *et al.* Convergent gene pairs restrict chromatin looping in Dictyostelium discoideum, acting as directional barriers for extrusion. Preprint at https://doi.org/10.1101/2024.06.12.598618 (2024).
38. Belokopytova, P. & Fishman, V. Predicting Genome Architecture: Challenges and Solutions. *Front. Genet.* **11**, 617202 (2021).
39. Rowley, M. J. & Corces, V. G. Organizational principles of 3D genome architecture. *Nat Rev Genet* **19**, 789–800 (2018).
40. Du, Z. *et al.* Polycomb group proteins regulate chromatin architecture in mouse oocytes and early embryos. *Molecular Cell* **77**, 825-839.e7 (2020).
41. Flyamer, I. M. *et al.* Single-nucleus Hi-C reveals unique chromatin reorganization at oocyte-to-zygote transition. *Nature* **544**, 110–114 (2017).
42. Wang, Y. *et al.* Reprogramming of meiotic chromatin architecture during spermatogenesis. *Molecular Cell* **73**, 547-561.e6 (2019).
43. Cheng, G. *et al.* High resolution maps of chromatin reorganization through mouse meiosis reveal novel features of the 3D meiotic structure. Preprint at https://doi.org/10.1101/2024.03.25.586627 (2024).

1172 44. Krasikova, A., Khodyuchenko, T., Maslova, A. & Vasilevskaya, E. Three-dimensional organisation of
1173 RNA-processing machinery in avian growing oocyte nucleus. *Chromosome Res* **20**, 979–994
1174 (2012).
1175 45. Maslova, A. V. & Krasikova, A. V. Spatial arrangement of macro-, midi-, and microchromosomes in
1176 transcriptionally active nuclei of growing oocytes in birds of the order galliformes. *Cell Tiss. Biol.* **5**,
1177 281–293 (2011).
1178 46. Vlad, M. & Macgregor, H. C. Chromomere number and its genetic significance in lampbrush
1179 chromosomes. *Chromosoma* **50**, 327–347 (1975).
1180 47. Macgregor, H. C. Chromomeres revisited. *Chromosome Res* **20**, 911–924 (2012).
1181 48. Krasikova, A., Fishman, V. & Kulikova, T. Lampbrush chromosome studies in the post-genomic era.
1182 *BioEssays* **45**, 2200250 (2023).
1183 49. Gall, J. G. Transcription in the *Xenopus* Oocyte Nucleus. in *Xenopus Development* (eds. Kloc, M. &
1184 Kubiak, J. Z.) 3–15 (Wiley, 2014). doi:10.1002/9781118492833.ch1.
1185 50. Morgan, G. T. Imaging the dynamics of transcription loops in living chromosomes. *Chromosoma*
1186 **127**, 361–374 (2018).
1187 51. Kaufmann, R., Cremer, C. & Gall, J. G. Superresolution imaging of transcription units on newt
1188 lampbrush chromosomes. *Chromosome Res* **20**, 1009–1015 (2012).
1189 52. Mirny, L. A. & Solovei, I. Keeping chromatin in the loop(s). *Nat Rev Mol Cell Biol* **22**, 439–440
1190 (2021).
1191 53. Keinath, M. C., Davidian, A., Timoshevskiy, V., Timoshevskaya, N. & Gall, J. G. Characterization of
1192 axolotl lampbrush chromosomes by fluorescence in situ hybridization and immunostaining.
1193 *Experimental Cell Research* **401**, 112523 (2021).
1194 54. Kulikova, T., Maslova, A., Starshova, P., Rodriguez Ramos, J. S. & Krasikova, A. Comparison of the
1195 somatic TADs and lampbrush chromomere-loop complexes in transcriptionally active prophase I
1196 oocytes. *Chromosoma* **131**, 207–223 (2022).
1197 55. Kulikova, T. & Krasikova, A. RNA-FISH—on Lampbrush Chromosomes: Visualization of Individual
1198 Transcription Units. in *Cytogenetics and Molecular Cytogenetics* 307–317 (CRC Press, Boca Raton,
1199 2022). doi:10.1201/9781003223658-26.
1200 56. Krasikova, A. *et al.* The first chicken oocyte nucleus whole transcriptomic profile defines the
1201 spectrum of maternal mRNA and non-coding RNA genes transcribed by the lampbrush
1202 chromosomes. *Nucleic Acids Research* **52**, 12850–12877 (2024).
1203 57. Zlotina, A. *et al.* New insights into chromomere organization provided by lampbrush chromosome
1204 microdissection and high-throughput sequencing. *Front. Genet.* **11**, 57 (2020).
1205 58. Zlotina, A., Kulikova, T., Kosyakova, N., Liehr, T. & Krasikova, A. Microdissection of lampbrush
1206 chromosomes as an approach for generation of locus-specific FISH-probes and samples for high-
1207 throughput sequencing. *BMC Genomics* **17**, 126 (2016).
1208 59. Kulikova, T., Surkova, A., Zlotina, A. & Krasikova, A. Mapping epigenetic modifications on chicken
1209 lampbrush chromosomes. *Mol Cytogenet* **13**, 32 (2020).
1210 60. Krasikova, A., Kulikova, T., Rodriguez Ramos, J. S. & Maslova, A. Assignment of the somatic A/B
1211 compartments to chromatin domains in giant transcriptionally active lampbrush chromosomes.
1212 *Epigenetics & Chromatin* **16**, 24 (2023).
1213 61. Krasikova, A. V. & Kulikova, T. V. Distribution of heterochromatin markers in lampbrush
1214 chromosomes in birds. *Russ J Genet* **53**, 1022–1029 (2017).
1215 62. Gridina, M. *et al.* Comparison and critical assessment of single-cell Hi-C protocols. *Heliyon* **8**,
1216 e11023 (2022).
1217 63. Galitsyna, A. A. & Gelfand, M. S. Single-cell Hi-C data analysis: safety in numbers. *Briefings in*
1218 *Bioinformatics* **22**, bbab316 (2021).
1219 64. Akgol Oksuz, B. *et al.* Systematic evaluation of chromosome conformation capture assays. *Nat*
1220 *Methods* **18**, 1046–1055 (2021).
1221 65. Rao, S. S. P. *et al.* A 3D Map of the Human Genome at Kilobase Resolution Reveals Principles of
1222 Chromatin Looping. *Cell* **159**, 1665–1680 (2014).
1223 66. Nurislamov, A., Lagunov, T., Gridina, M., Krasikova, A. & Fishman, V. Single-cell DNA methylation
1224 analysis of chicken lampbrush chromosomes. *IJMS* **23**, 12601 (2022).
1225 67. Zlotina, A. *et al.* Centromere positions in chicken and Japanese quail chromosomes: de novo
1226 centromere formation versus pericentric inversions. *Chromosome Res* **20**, 1017–1032 (2012).
1227 68. Krasikova, A., Barbero, J. L. & Gaginskaya, E. Cohesion proteins are present in centromere protein
1228 bodies associated with avian lampbrush chromosomes. *Chromosome Res* **13**, 675–685 (2005).
1229 69. Beenders, B., Watrin, E., Legagneux, V., Kireev, I. & Bellini, M. Distribution of XCAP-E and XCAP-
1230 D2 in the Xenopus oocyte nucleus. *Chromosome Research* **11**, 549–564 (2003).
1231 70. Li, D. *et al.* Comparative 3D genome architecture in vertebrates. *BMC Biol* **20**, 99 (2022).
1232 71. Jerković, I. *et al.* Genome-wide binding of posterior HOXA/D transcription factors reveals
1233 subgrouping and association with CTCF. *PLoS Genet* **13**, e1006567 (2017).

72. Huang, Z. *et al.* Evolutionary analysis of a complete chicken genome. *Proc. Natl. Acad. Sci. U.S.A.* **120**, e2216641120 (2023).
73. Degalez, F. *et al.* Enriched atlas of lncRNA and protein-coding genes for the GRCg7b chicken assembly and its functional annotation across 47 tissues. *Sci Rep* **14**, 6588 (2024).
74. Brandão, H. B., Ren, Z., Karaboja, X., Mirny, L. A. & Wang, X. DNA-loop-extruding SMC complexes can traverse one another in vivo. *Nat Struct Mol Biol* **28**, 642–651 (2021).
75. Marko, J. F. & Siggia, E. D. Polymer Models of Meiotic and Mitotic Chromosomes. *MBoC* **8**, 2217–2231 (1997).
76. Maslova, A. & Krasikova, A. Nuclear actin depolymerization in transcriptionally active avian and amphibian oocytes leads to collapse of intranuclear structures. *Nucleus* **3**, 300–311 (2012).
77. Flemming, W. *Zellsubstanz, Kern Und Zelltheilung*. (Vogel, 1882).
78. Rückert, J. *Zur Entwickelungsgeschichte Des Ovarialeies Bei Selachiern*. (1892).
79. Leidescher, S. *et al.* Spatial organization of transcribed eukaryotic genes. *Nat Cell Biol* **24**, 327–339 (2022).
80. Morgan, G. T., Jones, P. & Bellini, M. Association of modified cytosines and the methylated DNA-binding protein MeCP2 with distinctive structural domains of lampbrush chromatin. *Chromosome Res* **20**, 925–942 (2012).
81. Franke, W. W., Scheer, U., Trendelenburg, M. F., Spring, H. & Zentgraf, H. Absence of nucleosomes in transcriptionally active chromatin. (1976).
82. Ocampo-Hafalla, M., Muñoz, S., Samora, C. P. & Uhlmann, F. Evidence for cohesin sliding along budding yeast chromosomes. *Open Biol.* **6**, 150178 (2016).
83. Davidson, I. F. *et al.* Rapid movement and transcriptional re-localization of human cohesin on DNA. *The EMBO Journal* **35**, 2671–2685 (2016).
84. Guérin, T. M., Barrington, C., Pobegalov, G., Molodtsov, M. I. & Uhlmann, F. An extrinsic motor directs chromatin loop formation by cohesin. *EMBO J* **43**, 4173–4196 (2024).
85. Bastié, N. *et al.* Sister chromatid cohesion halts DNA loop expansion. *Molecular Cell* **84**, 1139-1148.e5 (2024).
86. Gaginskaya, E., Kulikova, T. & Krasikova, A. Avian lampbrush chromosomes: a powerful tool for exploration of genome expression. *Cytogenet Genome Res* **124**, 251–267 (2009).
87. Krasikova, A. & Kulikova, T. *Hromosomy Tipa Lampovyh Shchetok: Sovremennye Predstavleniya i Perspektivy Issledovanij [Lampbrush Chromosomes: Current Insights and Research Perspectives]*. (St Petersburg: St Petersburg University Publishing House, 2019).
88. Krasikova, A. Centromernye rajony hromosom i associirovannye s nimi struktury v yadrah rastushchih oocitov ptic [Centromeric regions of chromosomes and associated structures in the nuclei of growing avian oocytes]. Ph. D. Thesis. (Saint Petersburg State University, Saint Petersburg, 2007).
89. Samejima, K. *et al.* Rules of engagement for condensins and cohesins guide mitotic chromosome formation. Preprint at https://doi.org/10.1101/2024.04.18.590027 (2024).
90. Wang, M. D. *et al.* Force and velocity measured for single molecules of RNA polymerase. *Science* **282**, 902–907 (1998).
91. Kong, M. *et al.* Human condensin I and II drive extensive ATP-dependent compaction of nucleosome-bound DNA. *Molecular Cell* **79**, 99-114.e9 (2020).
92. Ulianov, S. V. *et al.* Active chromatin and transcription play a key role in chromosome partitioning into topologically associating domains. *Genome Res.* **26**, 70–84 (2016).
93. Winick-Ng, W. *et al.* Cell-type specialization is encoded by specific chromatin topologies. *Nature* **599**, 684–691 (2021).
94. Eagen, K. P., Hartl, T. A. & Kornberg, R. D. Stable chromosome condensation revealed by chromosome conformation capture. *Cell* **163**, 934–946 (2015).
95. Stadler, M. R., Haines, J. E. & Eisen, M. B. Convergence of topological domain boundaries, insulators, and polytene interbands revealed by high-resolution mapping of chromatin contacts in the early Drosophila melanogaster embryo. *eLife* **6**, e29550 (2017).
96. Kolesnikova, T. D. Banding pattern of polytene chromosomes as a representation of universal principles of chromatin organization into topological domains. *Biochemistry Moscow* **83**, 338–349 (2018).
97. *Guide for the Care and Use of Laboratory Animals: Eighth Edition*. 12910 (National Academies Press, Washington, D.C., 2011). doi:10.17226/12910.
98. Martin, M. Cutadapt removes adapter sequences from high-throughput sequencing reads. *EMBnet j.* **17**, 10 (2011).
99. Durand, N. C. *et al.* Juicer Provides a One-Click System for Analyzing Loop-Resolution Hi-C Experiments. *Cell Systems* **3**, 95–98 (2016).
100. Gridina, M. *et al.* A cookbook for DNase Hi-C. *Epigenetics & Chromatin* **14**, 15 (2021).
101. Abdennur, N. & Mirny, L. A. Cooler: scalable storage for Hi-C data and other genomically labeled arrays. *Bioinformatics* **36**, 311–316 (2020).

1297 102. Flyamer, I. M., Illingworth, R. S. & Bickmore, W. A. *Coolpup.py:* versatile pile-up analysis of Hi-C
1298 data. *Bioinformatics* **36**, 2980–2985 (2020).
1299 103. Open2C *et al.* Cooltools: enabling high-resolution Hi-C analysis in Python. Preprint at
1300 https://doi.org/10.1101/2022.10.31.514564 (2022).
1301 104. Krueger, F., Kreck, B., Franke, A. & Andrews, S. R. DNA methylome analysis using short bisulfite
1302 sequencing data. *Nat Methods* **9**, 145–151 (2012).
1303 105. Krueger, F. & Andrews, S. R. Bismark: a flexible aligner and methylation caller for Bisulfite-Seq
1304 applications. *Bioinformatics* **27**, 1571–1572 (2011).
1305 106. Ferragina, P. & Manzini, G. Opportunistic data structures with applications. in *Proceedings 41st*
1306 *Annual Symposium on Foundations of Computer Science* 390–398 (IEEE Comput. Soc, Redondo
1307 Beach, CA, USA, 2000). doi:10.1109/SFCS.2000.892127.
1308 107. Langmead, B. & Salzberg, S. L. Fast gapped-read alignment with Bowtie 2. *Nat Methods* **9**, 357–
1309 359 (2012).
1310 108. Langmead, B., Trapnell, C., Pop, M. & Salzberg, S. L. Ultrafast and memory-efficient alignment of
1311 short DNA sequences to the human genome. *Genome Biol* **10**, R25 (2009).
1312 109. Langmead, B., Wilks, C., Antonescu, V. & Charles, R. Scaling read aligners to hundreds of threads
1313 on general-purpose processors. *Bioinformatics* **35**, 421–432 (2019).
1314 110. Kim, D., Paggi, J. M., Park, C., Bennett, C. & Salzberg, S. L. Graph-based genome alignment and
1315 genotyping with HISAT2 and HISAT-genotype. *Nat Biotechnol* **37**, 907–915 (2019).
1316 111. Danecek, P. *et al.* Twelve years of SAMtools and BCFtools. *GigaScience* **10**, giab008 (2021).
1317 112. Shumate, A., Wong, B., Pertea, G. & Pertea, M. Improved transcriptome assembly using a hybrid of
1318 long and short reads with StringTie. *PLoS Comput Biol* **18**, e1009730 (2022).
1319 113. Solovei, I., Gaginskaya, E., Allen, T. & Macgregor, H. A novel structure associated with a lampbrush
1320 chromosome in the chicken, *Gallus domesticus*. *Journal of Cell Science* **101**, 759–772 (1992).
1321 114. Cremer, M. *et al.* Multicolor 3D Fluorescence In Situ Hybridization for Imaging Interphase
1322 Chromosomes. in *The Nucleus* (ed. Hancock, R.) vol. 463 205–239 (Humana Press, Totowa, NJ,
1323 2012).
1324 115. Zlotina, A. & Krasikova, A. FISH in Lampbrush Chromosomes. in *Fluorescence In Situ Hybridization*
1325 *(FISH)* (ed. Liehr, T.) 445–457 (Springer Berlin Heidelberg, Berlin, Heidelberg, 2017).
1326 doi:10.1007/978-3-662-52959-1_45.
1327 116. Krasikova, A., Kulikova, T., Saifitdinova, A., Derjusheva, S. & Gaginskaya, E. Centromeric protein
1328 bodies on avian lampbrush chromosomes contain a protein detectable with an antibody against
1329 DNA topoisomerase II. *Chromosoma* **113**, 316–323 (2004).
1330 117. Imakaev, M., Goloborodko, A., & Hbbrandao. mirnylab/polychrom: v0.1.0.
1331 https://doi.org/10.5281/ZENODO.3579472 (2019).
1332 118. Pradhan, B. *et al.* SMC complexes can traverse physical roadblocks bigger than their ring size. *Cell*
1333 *Reports* **41**, 111491 (2022).
1334 119. Ryu, J.-K. *et al.* Condensin extrudes DNA loops in steps up to hundreds of base pairs that are
1335 generated by ATP binding events. *Nucleic Acids Research* **50**, 820–832 (2022).
1336